X-ray fluorescence core scanning records of chemical weathering and monsoon evolution over the past 5 Myr in the southern South China Sea

Jun Tian,[1] Xin Xie,[1] Wentao Ma,[1] Haiyan Jin,[1] and Pinxian Wang[1]

Received 13 August 2010; revised 1 April 2011; accepted 13 July 2011; published 12 October 2011.

[1] We present ultrahigh resolution K/Al and Ti/Al records at ODP Site 1143 for the past 5 Myr, which were obtained by nondestructive X-ray fluorescence (XRF) core scanning on the sediment surface of the archive half cores of this site at a step of 1 cm. The K/Al and Ti/Al records and their amplitudes of the variability on glacial/interglacial cycles show a markedly increasing trend since ~2.5 Ma, indicating a gradual strengthening of the chemical weathering and the East Asian summer monsoon under the influences from the Northern Hemisphere glaciation (NHG). Evolutive cross spectral analyses of K/Al with benthic foraminiferal $\delta^{18}O$ reveal that phases of the East Asian summer monsoon abruptly changed by more than 90° at 4.0 Ma, 2.75 Ma, 1.0 Ma and 0.6 Ma relative to global ice volume at the obliquity and the precession bands over the past 5 Myr. Strong 400 kyr and 100 kyr cycles in the K/Al and Ti/Al records consistently exist over the past 5 Myr. Particularly, these cycles are highly coherent with the long and short eccentricity cycles in the truncated insolation at 65°N, indicating an eccentricity forcing of the East Asian summer monsoon. The chemical weathering recorded in the elemental records of ODP Site 1143 also shows highly coherent relationship with the ocean carbon reservoir at the eccentricity, the obliquity and the precession bands over the late Pliocene and Pleistocene.

Citation: Tian, J., X. Xie, W. Ma, H. Jin, and P. Wang (2011), X-ray fluorescence core scanning records of chemical weathering and monsoon evolution over the past 5 Myr in the southern South China Sea, *Paleoceanography*, *26*, PA4202, doi:10.1029/2010PA002045.

1. Introduction

[2] Chemical weathering acts as vital components in the biogeochemical box models through modulating the size of oceanic carbon reservoir [*Walker and Kasting*, 1992; *Pälike et al.*, 2006; *Merico et al.*, 2008]. Geological records reveal that secular changes in chemical weathering are tightly related to long-term changes in the atmospheric CO_2 concentration over the Cenozoic [*Raymo and Ruddiman*, 1992; *Haug et al.*, 1999]. Understanding the relationship between chemical weathering and the control factors is of great importance in clarifying the mechanism of global carbon cycle.

[3] Chemical weathering on land is partly controlled by precipitation [*Kump et al.*, 2000]. The precipitation in East Asia and India is mainly controlled by Asian summer monsoons which transport moisture from the oceans to the continent. Studying the East Asian summer monsoon evolution through geological time by proxy records of chemical weathering such as K/Al and Ti/Al of the deep sea sediments from the South China Sea has been successfully attempted by several researchers [*Wehausen and Brumsack*, 2002; *Wei et al.*, 2006; *Clift et al.*, 2008]. Investigating the chemical weathering variability is of great help in clarifying the process of the Asian summer monsoon evolution.

[4] Besides tectonics which is an important control on chemical weathering [*Raymo et al.*, 1988], climate, a process internal to the surface Earth system, governs erosion and associated terrigenous sedimentation rates throughout the world by controlling the abundances and distribution of the continental rivers and glaciers, the primary erosive agents [*Zhang et al.*, 2001]. Significant changes of erosion rates in the late Cenozoic have been proved to be closely related to the major expansions of continental ice sheet. For example, chemical weathering proxy records (e.g., K/Al) of sediments from the South China Sea, Bay of Bengal and Arabian Sea indicate the erosional history of Himalaya over the past 23 Myr and a rapid strengthening at ~15 Ma [*Clift et al.*, 2008], which is nearly synchronous with the onset of the East Antarctic Ice Sheet expansion [*Shevenell et al.*, 2004, 2008]. About 2–4 Ma ago, sediment accumulation rates throughout the world greatly increased due to remarkable increases of erosion rates on sea level change affected continental margins - such as on the Mississippi delta, and on sea level change unaffected high Asia region - such as on the Tibet and the regions surrounding Tibet [*Zhang et al.*, 2001]. During

[1]State Key Laboratory of Marine Geology, Tongji University, Shanghai, China.

0883-8305/11/2010PA002045

this period, the most significant increase in the accumulation rate happens at ~2.7 Ma ago, synchronizing with the abrupt expansion of the Northern Hemisphere ice sheet [*Haug and Tiedemann*, 1998; *Tian et al.*, 2002, 2006].

[5] As external forcing, the Earth's orbital geometry should have played a great role in controlling the chemical weathering change throughout the Cenozoic [*Zachos et al.*, 2001; *Pälike et al.*, 2006]. Consistent imprints of the eccentricity, the obliquity and the precession have remained in the ocean carbon reservoir as recorded in the benthic and planktonic foraminiferal $\delta^{13}C$. Over the past 5 Myr, 12 $\delta^{13}C_{max}$ events have paced the foraminiferal $\delta^{13}C$ records from the global oceans [*Wang et al.*, 2010]. The $\delta^{13}C_{max}$ events particularly correspond to the eccentricity minimum, displaying prominent 400 kyr long eccentricity cycles [*Wang et al.*, 2010]. As a major factor modulating the size of ocean carbon reservoir, the chemical weathering should also show close connection with the 400 kyr long eccentricity cycle. Investigating this long-term change in chemical weathering is of great help in clarifying the mechanism of global carbon cycle.

[6] Reconstruction of proxy records of chemical weathering from the deep sea sediments is usually based on elemental or mineralogical analyses using the traditional instruments such as Inductively Coupled Plasma Mass Spectroscopy (ICP-MS) and X-ray diffraction (XRD). However, low efficiency of these methods constrains reconstruction of long proxy records of chemical weathering with high resolution. Here we present 5 Myr long K/Al and Ti/Al records from ODP (Ocean Drilling Program) Site 1143 in the southern South China Sea with ultrahigh resolution (1 cm). These records which are derived from X-ray Fluorescence (XRF) core scanning on the Archive sediment cores are greatly helpful in uncovering the forcing mechanism of the chemical weathering evolution over the late Pliocene and the Pleistocene and also contribute to the understanding of the Asian summer monsoon variability.

2. Materials and Methods

2.1. Site Selection and Age Model

[7] ODP Site 1143 (9°21.72′N, 113°17.11′E, at a water depth of 2772 m) is located in the southern South China Sea, the biggest marginal sea from the western Pacific. Sediment at this site contains terrigenous fluxes from the Mekong River system, which drains a large area of the southeastern Asia and portions of the Tibetan Plateau [*Wang et al.*, 2000]. Terrigenous detritus from the other rivers such as the Molengraaff river in the Sunda shelf and rivers in Borneo, also contributes to the sediments at this site [*Wang et al.*, 1999].

[8] Previous studies at this site have established a precise age model over the past 5 Myr by tuning the benthic foraminiferal $\delta^{18}O$ to the obliquity and precession using the La93 [*Laskar et al.*, 1993] astronomical solution of Earth's geometry [*Tian et al.*, 2002]. In this study, we used the La2004 astronomical solution [*Laskar et al.*, 2004] as orbital forcing. The two astronomical solutions are nearly identical in the reconstruction of the eccentricity over the past 10 Myr, but are a little bit different in the reconstruction of the obliquity and the precession due to the change of the precession model in La2004 [*Laskar et al.*, 2004]. For example, the difference in the obliquity reconstruction between the two solutions amounts to ~2° over the past 20 Myr. But over the past 5 Myr, this difference is too small to bias our cross spectral analyses between proxy records and orbital forcing. All the spectral, cross spectral and Gauss band-pass filtering analyses are performed by using the software Analyseries 1.2 [*Paillard et al.*, 1996].

2.2. Provenance and Sources of the Sediments in the Southern South China Sea

[9] Distinguishing fluvial or eolian materials from terrigenous components of the hemipelagic sediments of ODP Site 1143 is important in excavating climate signals from the elemental data set of the sedimentary profile. Terrigenous material is deposited into the ocean via fluvial and eolian pathways [*Boyle*, 1983; *Yarincik et al.*, 2000]. Eolian fluxes transported into the ocean via monsoons or westerly or trade winds are controlled by the extent of aridity in source regions, wind strength and wind direction, being closely related to physical weathering in the source regions. Fluvial fluxes transported into the ocean via estuary are related to chemical weathering in the source regions especially the tropical warm and humid fluvial drainage basins. For example, the Al/Ti and K/Al ratios in bulk sediments from the Cariaco Basin in the tropical Atlantic reflect wind-blown source in the Saharan desert and hydrological condition in the Venezuelan riverine drainage basins [*Boyle*, 1983; *Yarincik et al.*, 2000; *Martinez et al.*, 2007, 2009, 2010].

[10] *Wang et al.* [1999] once carried out a study of the origins of the sediments from the northern and southern South China Sea using grain size analyses on the samples from several gravity and piston cores and on a series of modern hemipelagic surface sediment samples. Grain sizes (% clay <6 μm and the modal grain size of silt >6 μm) were measured on the carbonate-free siliciclastic sediment fraction which still includes a small but negligible portion of marine biogenic opal. Their results show that the clay fraction is dominating the hemipelagic sediment sections of the South China Sea. Particularly in the southern South China Sea, the clay content <6 μm amounts to 88–91% during the Holocene and increases to 93–95% during the cold stages 2–4. Based on the Koopmann grain-size index [*Koopmann*, 1981] which is the correlation of % clay plus fine silt (<6.3 μm) versus silt modal grain sizes (6.3–63 μm) in the siliciclastic, carbonate-free fraction (<63 μm), *Grothmann* [1996] identified three groups of samples from a variety of modern hemipelagic surface samples distributed in the South China Sea, namely, fluvial sediment discharge, eolian-dust input and sediment winnowing on the seafloor. Among these modern surface samples, most of those from the southern South China Sea are of fluvial origin [*Grothmann*, 1996]. Following the same method, *Wang et al.* [1999] found that sediments in the northern South China Sea cores (17940-1/2) have three origins of eolian, fluvial and winnowing whereas sediments in the southern South China Sea cores (17964-2/3) are purely of fluvial origin.

[11] ODP Site 1143 is very close to the core 17964 of which the water depth is 1556 m, much shallower than that of ODP Site 1143. Weight percent of the total terrigenous materials in bulk samples at ODP Site 1143 varies between 60% and 80% for the past 5 Myr, and relative percent of clay minerals in terrigenous components varies between 74% and 82% [*Wan et al.*, 2006]. Over the past 5 Myr, illite,

kaolinite, chlorite and smectite of the sediments of ODP Site 1143 don't show long-term changes but regular glacial/interglacial variations in their contents indicating stable source regions [*Wan et al.*, 2006]. Potential source regions of the clay minerals in the southern South China Sea are the Mekong Rivers, the Red rivers, the rivers in Borneo and the rivers in Indonesian islands [*Liu et al.*, 2007]. The clay mineral assemblage at ODP Site 1143 after 5.0 Ma is much similar to that of the surface sediment samples in the Mekong River estuary (average illite 47%, chlorite 23%, kaolinite 20% and smectite 10%) [*Liu et al.*, 2003], indicating that the Mekong drainage basin is the main source of the hemipelagic sediments in the southern South China Sea. Correlation of TiO_2 and Al_2O_3 contents of the Pliocene sediments from ODP Site 1143 indicates that samples at this site are characterized by relatively low TiO_2/Al_2O_3 ratios which is close to the data point for Mekong suspended matter, whereas ODP Site 1145 from the northern South China Sea samples are characterized by high TiO_2/Al_2O_3 ratios which is close to the dilution line for eolian loess [*Wehausen et al.*, 2003]. Other evidences from variations in immobile trace element ratios such as La/Th and Th/Yb and from the plot of La/Th versus Th/Yb of sediments from ODP Site 1143, the Mekong River, Pearl River, and rocks from Indonesian arc [*Sendjaja and Kimura*, 2010] also support the Mekong River being the most likely source regions of sediments at ODP Site 1143.

[12] Accordingly, the hemipelagic sediments at ODP Site 1143 should be of fluvial origin, with the Mekong rivers drainage basin being the primary and stable source. But as indicated by *Wehausen et al.* [2003], there seem to have been at least one other source with slightly higher Ti and lower Al contents delivering material to this part of the South China Sea, probably the Red river and the Pearl river as well as rivers in Boneo.

2.3. K/Al and Ti/Al Ratios as Indicators of Weathering Process

[13] Both potassium (K) and aluminum (Al) occur chiefly in the clay minerals, with lesser contribution from feldspars and zeolites, and potassium occurs chiefly in illite while aluminum is abundant in all clay minerals [*Boyle*, 1983]. Illite is generally a weathering product in temperate to arid climates where physical weathering is strong but chemical weathering is weak, while kaolinite is typically a product of chemical weathering in tropical, humid climates [*Boyle*, 1983; *Yarincik et al.*, 2000]. So, it is likely that variations in K/Al reflect the abundance of illite relative to kaolinite [*Boyle*, 1983]. Thus, ideally, given the bulk sediment is primarily made of clay minerals, a decrease in K/Al of the bulk sediment would indicate a decrease in illite content and an increase in kaolinite content which would indicate strengthened chemical weathering and weakened physical weathering. Titanium (Ti) is enriched in heavy minerals such as rutile, which is commonly associated with the coarser sediment fraction. Aluminum is a primary constituent of aluminosilicate minerals and the crustal component. Both Al and Ti do not respond to redox variations. Ti/Al is potentially representative of grain size, eolian source geochemistry, or both, as has been described in the Cariaco Basin [*Boyle*, 1983; *Yarincik et al.*, 2000; *Martinez et al.*, 2007, 2009, 2010].

[14] Unlike in the Cariaco basin, the usage of K/Al and Ti/Al of the bulk sediments as weathering indicators is more complicated in the southern South China Sea. Apparently, the Ti content in the sediment of ODP Site 1143 is more of fluvial origin than eolian origin, and thus the Ti/Al here is not an indication of eolian source geochemistry in the central Asia. The indication of K/Al in chemical weathering process is also different from that in the Arabian Sea [*Clift et al.*, 2008] and the discussion above. As commonly recognized, some mobile elements like Na, Ca, and Sr which can be easily removed from parent rocks and sediments are generally depleted in weathering products while other mobile elements like K, Rb, Mg and Ba which can be easily leached off primary minerals but then can be fixed by secondary clay minerals in weathering profiles are usually enriched in the weathering products after moderate weathering process [*Nesbitt et al.*, 1980; *Nesbitt and Markovics*, 1997; *Wei et al.*, 2006; *Clift et al.*, 2008]. Some immobile elements like Al, Fe, Ti and Zr are generally conservative during chemical weathering processes, tending to be enriched or keeping constant in weathering products [*Nesbitt and Markovics*, 1997; *Nesbitt et al.*, 1980; *Wei et al.*, 2006]. Behaviors of some elements can change under different chemical weathering intensity. For example, elements like K, Rb, Ti and Zr tend to be enriched in weathering products after moderate chemical weathering process but become depleted after extreme chemical weathering process [*Wei et al.*, 2006]. Clay mineralogical analyses, Rb, Sr, and Nd concentration and Sr-Nd isotopic results in 93 modern argillaceous samples collected from drainage basins of the Pearl, Red, and Mekong rivers, indicate intensive silicate weathering in the Pearl River basin, moderate to intensive in the Mekong River basin, and moderate in the Red River basin [*Liu et al.*, 2007]. On glacial/interglacial timescale, the K/Al and Ti/Al records of ODP Site 1143 generally show large values during interglacial periods and small values during glacial values (Figure 3). These evidences clearly indicate that increase in K/Al or Ti/Al at ODP Site 1143 is probably related to the intensified chemical weathering. Other proxies from the South China Sea such as the CIA and the C_{RAT} as well as the K/Al and Ti/Al have once been used to indicate variations in chemical weathering intensity [*Nesbitt and Markovics*, 1997; *Wei et al.*, 2006; *Clift et al.*, 2008]. CIA is defined as the percentage of Al_2O_3 in (Al_2O_3 + CaO + Na_2O + K_2O) using molecular proportions [*Nesbitt and Young*, 1982]. The CIA is susceptible to variations linked to sediment mineralogy and provenance evolution. Sands yield lower CIA values compared to clays in the same drainage system [*Clift et al.*, 2008]. C_{RAT} is defined as the mineralogical ratio of chlorite versus (chlorite + haematite + goethite). The alteration minerals hematite and goethite are largely produced by chemical weathering, whereas chlorite is more produced by physical weathering. Thus, C_{RAT} proxy tracks the degree of chemical weathering in the source region, with low values indicating strong chemical weathering and high values indicating weak chemical weathering. C_{RAT} is more sensitive to the clay minerals than CIA. The C_{RAT} and K/Al have been proved to be more effective in indicating the chemical weathering process in the Asian continent than the CIA [*Clift et al.*, 2008]. For example, the C_{RAT} record from the South China Sea and the Bengal fan are consistent with each other in the Neogene period, and so do the K/Al records from the two locations. However, the CIA shows close correlation with the C_{RAT} and K/Al only in the Bengal fan but it conflicts

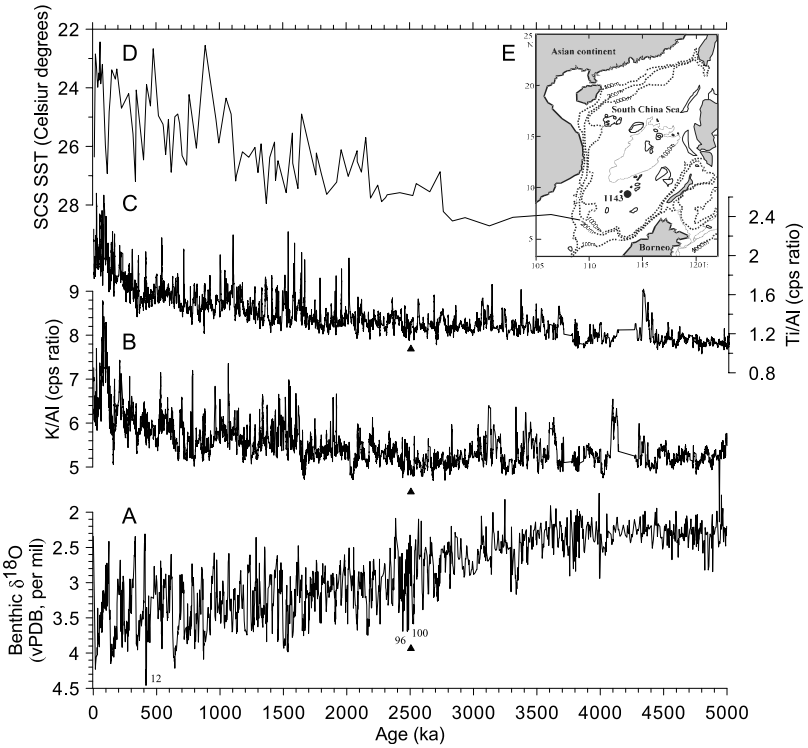

Figure 1. Climate proxy records from the South China Sea over the past 5 Myr. (a) Benthic foraminiferal $\delta^{18}O$ at ODP Site 1143 from the southern South China Sea [*Tian et al.*, 2002]; (b) K/Al (cps ratio) at ODP Site 1143 (11-point Gauss smoothing); (c) Ti/Al (cps ratio) at ODP Site 1143 (11-point Gauss smoothing); (d) $U^{k'}_{37}$ SST (sea surface temperatures) at ODP Site 1147/1148 from the northern South China Sea [*Jia et al.*, 2008]; (e) location map of ODP Site 1143. Numbers in Figure 1a denote Marine Isotope Stages (MIS). The triangles point to the onset of the Northern Hemisphere glaciation (NHG) at ~2.5 Ma.

with the C_{RAT} and K/Al at ODP Site 1148 in the South China Sea [*Wei et al.*, 2006; *Clift et al.*, 2008]. Here, in the Bengal fan and the South China Sea, K/Al resembles C_{RAT} in long and short-term variations, with increased K/Al indicating wetter condition and thus the intensified chemical weathering [*Clift et al.*, 2008].

[15] As indicated by *Wehausen et al.* [2003], weathering may explain changes in the Al contents but not in the Si and Ti contents in the southern South China Sea. A combined influence from both climate-related factors and oceanographic-related factors probably controls variations in the Ti/Al ratio of the hemipelagic sediments of ODP Site 1143. This indicates that Ti/Al may be more complicated than K/Al in implying the chemical weathering intensity changes. However, the Ti/Al and K/Al records at ODP Site 1143 resemble each other in both long-term variations and glacial/interglacial cycles (Figure 1). The secular variations of both ratios show different patterns than that of the ice-volume controlled sea level change as displayed in the benthic $\delta^{18}O$ record (Figure 1). This resemblance indicates that Ti/Al proxy also tracks the chemical weathering intensity as K/Al in the southern South China Sea, although we need further intensive work to clarify the physical and chemical mechanisms behind this ratio.

2.4. XRF Core Scanning

[16] We performed X-ray fluorescence (XRF) core scanner measurements on the archive cores of ODP Site 1143 in the southern South China Sea in Tongji University, Shanghai, China. The scanning was performed with a step of 1 cm between 0.06 and 190.77 m composite depth (mcd), the same depth interval as that for the benthic foraminiferal stable oxygen and carbon isotopic measurements at the same Site which spans the past 5 Myr [*Tian et al.*, 2002]. The Avvatech XRF Core Scanner in Tongji University allows continuous and non-destructive analysis of elements ranging from Aluminum (Al, atomic number 13) through to Uranium (U, atomic number 92) [*Richter et al.*, 2006]. The basic unit of the XRF core scanner measurements is total counts or counts per second (cps). This unit implies the elemental intensity which is proportional to the chemical concentrations [*Tjallingii et al.*, 2007]. Mineral heterogeneities and surface roughness effects are usually minimized by the relatively large irradiated area (1 cm^2) of the core scanner for fine-grained sediments [*Jansen et al.*, 1998]. A comparative study of XRF core scanner measurements with conventional XRF analyses on discrete and homogenized samples from the deep sea core GeoB7920 in the western tropical Atlantic indicates that the cohesive and adhesive properties of water cause the formation of a thin water film between the sediment surface and the foil in soft marine sediments, and that this water film artificially enhances the water content in the sample volume analyzed by the XRF core scanner which strongly reduces the element intensities of the lighter element Al and Si [*Tjallingii et al.*, 2007]. This disadvantage together with other reasons like irregularities of the split core surface

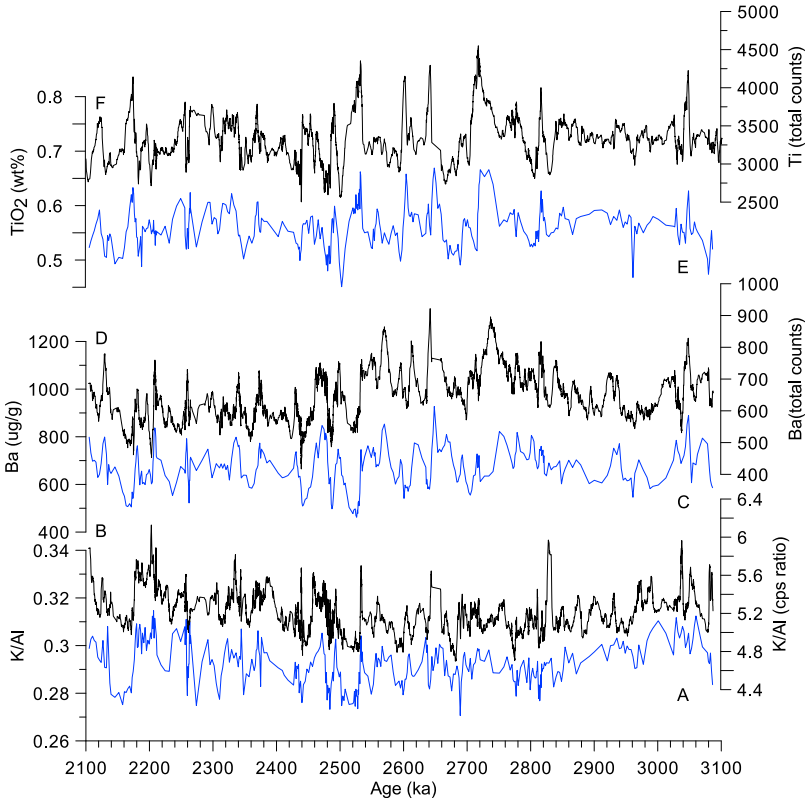

Figure 2. Comparison of Ti, Ba, and K/Al records measured by XRF core scanning on the archive core surface (black lines) with the same elemental records measured by conventional X-ray fluorescence analyses on the dry bulk samples (blue lines [*Wehausen and Brumsack*, 2002]) (2.1–3.1 Ma). (a) K/Al ratio of *Wehausen and Brumsack* [2002]; (b) K/Al (cps ratio) of this study; (c) Ba of *Wehausen and Brumsack* [2002]; (d) Ba (cps) of this study; (e) TiO_2 of *Wehausen and Brumsack.* [2002]; (f) Ti (cps) of this study.

makes it difficult to transfer the core-scanner output to the real elemental concentration [*Weltje and Tjallingii*, 2008]. Despite this problem the XRF core scanner measurement has the ability to reflect similar or even identical cyclic changes and long-term trend of the main major and minor elements to that of the measurements obtained by conventional XRF analyses, which can be evidenced by the comparative study made by *Tjallingii et al.* [2007]. In a word, XRF core scanner measurements provide high quality data set for high resolution time series reconstruction and stratigraphic correlations, allowing detailed sedimentary and climatic reconstructions on centennial to millennial [*Yancheva et al.*, 2007], orbital [*Westerhold et al.*, 2007] and tectonic timescales [*Clift et al.*, 2008]. The K/Al and Ti/Al records used in comparison and each numerical analysis are smoothed records by 11 points Gauss smoothing.

3. Results

3.1. Comparison of Elemental Records Between XRF Core Scanner and Conventional Measurements

[17] *Wehausen et al.* [2003] made conventional X-ray fluorescence analyses on the dry bulk samples at Site 1143 between 99.5 and 136.46 mcd, with a resolution of 10 cm, one tenth the resolution of our XRF core scanner measurements over the same interval. According to the age model of *Tian et al.* [2002], this depth interval corresponds to the time interval 2.104–3.086 Ma. To check the reliability of our XRF core scanning results, we make 11-point Gaussian smoothing on the Ba, Ti and K/Al records, and then compare them with the same elemental records of *Wehausen et al.* [2003] obtained by conventional XRF analyzer (Figure 2). The visual comparison shows that two kinds of Ba, Ti and K/Al are in good agreement in both the secular changes and the glacial/interglacial cycles. Even the timing of the transition from glacial to interglacial is identical to each other in most cases (Figure 2). Other elements like Ca also show great similarities in the glacial cycles and secular changes between the two methods over the past 5 Myr (Z. Liu, personal communication, 2010).

[18] Some differences still exist in the comparison. For example, the units of the elemental records are different in the two kinds of measurements. In the conventional XRF (X-ray fluorescence) analyses, the basic unit denotes the elemental concentration which is usually recorded as weight percent of one element relative to the total weights (wt%) on a carbonate-free basis (cfb); whereas in the XRF core scanner measurements, the basic unit denotes the counts per second (cps) which is usually proportional to the real chemical concentration of the measured element. The range of K/Al ratio also shows big discrepancy in the two records, with one varying between 0.27 and 0.31 for the conventional XRF analyses but the other between 4.9 and 6.2 for the XRF core scanner measurements (Figure 2). The relative concentration

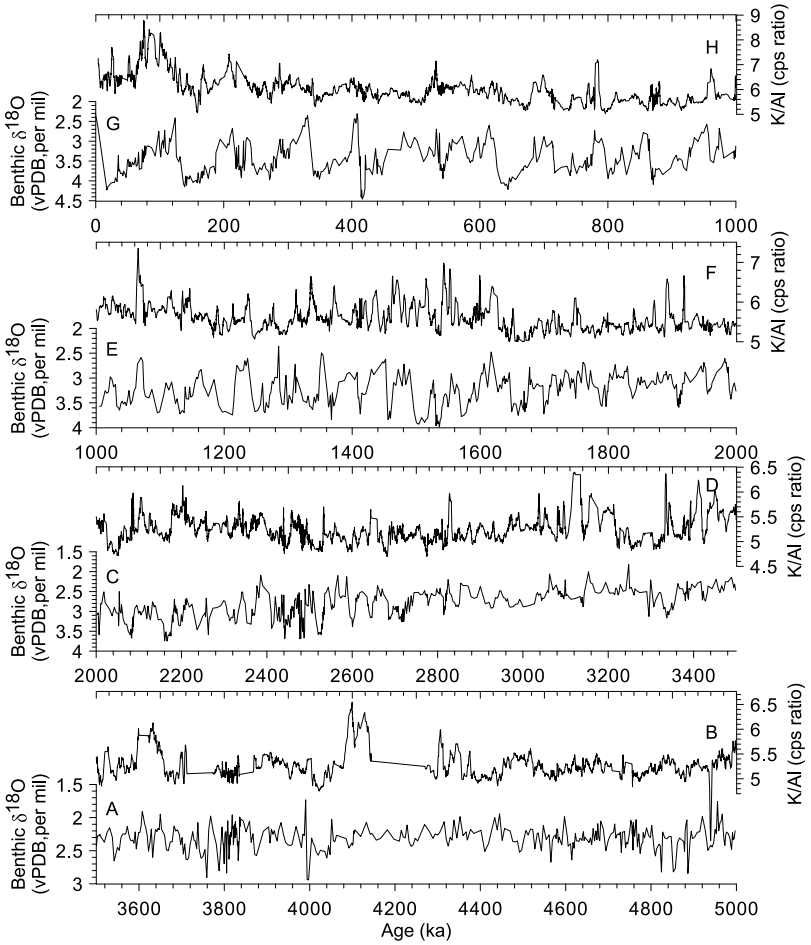

Figure 3. Benthic foraminiferal δ^{18}O [*Tian et al.*, 2002] and K/Al (cps ratio) at ODP Site 1143 from the southern South China Sea (0–5 Ma): (a, c, e, and g) δ^{18}O and (b, d, f, and h) K/Al (cps ratio).

of one element such as K compared with the other element such as Al is probably incorrectly recorded in the XRF core scanner measurements, but the basically temporal change of one element is correctly recorded in these records and so do the most of the elemental ratios such as K/Al and Ti/Al. Because quantitative calibration of counts per second to the real concentration unit of the element is complex [*Weltje and Tjallingii*, 2008] and we are doing an application in paleoceanography not geochemistry, the major elemental records and some of the minor elemental records obtained by the XRF core scanner measurements should be sufficient. On the whole, the XRF core scanner measurements at ODP Site 1143 appear to be reliable proxy records in revealing the long-term trend and glacial/interglacial cycles of paleoenvironmental changes.

3.2. Variability of K/Al and Ti/Al for the Past 5 Myr

[19] The K/Al and Ti/Al show similar patterns in the secular changes (Figures 1b and 1c), with gradually increasing trend for the past 5 Myr. On orbital timescale, both the K/Al and Ti/Al records show nearly the same glacial/interglacial cycles. Some minor differences also exist in the two records. For example, a notable spike occurs in the K/Al record at ~4.1 Ma but it is absent in the Ti/Al record. In general, the K/Al and Ti/Al perform similar glacial/interglacial cycles as that of the benthic foraminiferal δ^{18}O over the past 5 Myr (Figure 3). But, these glacial cycles in the elemental records do not show a consistent pattern. During some glacials like MIS (Marine Isotope Stage) 6, the K/Al shows low values, but during other glacials it shows high values. Within a glacial cycle, the timing of the peak values is sometimes different in the K/Al and the δ^{18}O. For example, the most climate proxy records like the benthic foraminiferal δ^{18}O show the biggest values at MIS 5.5 (Figure 3), but this peak value in the K/Al doesn't occur at MIS 5.5 but lags for ~50–60 kyr behind. These features indicate that there exist variable phases of the K/Al and Ti/Al relative to the δ^{18}O. We will discuss the significance of the variable phases in climate change in the following text.

4. Discussion

4.1. Northern Hemisphere Glaciation Forcing

4.1.1. Onset of Northern Hemisphere Glaciation and Mid-Pleistocene Revolution

[20] The benthic foraminiferal δ^{18}O of ODP Site 1143 has clearly documented the waxing and waning of the Northern Hemisphere ice sheet for the past 5 Myr (Figures 1 and 3). As pointed out previously [*Tian et al.*, 2002, 2006], a prominent increase of the glacial benthic δ^{18}O of ODP Site

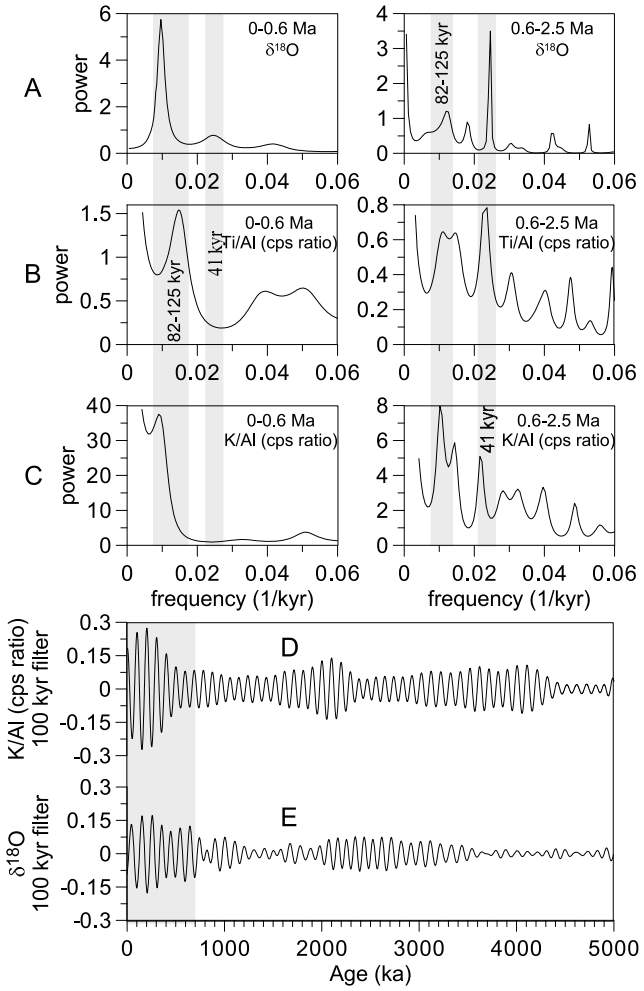

Figure 4. Maximum Entropy spectral analyses of (a) benthic foraminiferal $\delta^{18}O$, (b) Ti/Al (cps ratio), and (c) K/Al (cps ratio), and Gauss band-pass filtering analyses at the 100 kyr band on (d) K/Al (cps ratio) and (e) benthic foraminiferal $\delta^{18}O$. The spectral analyses are performed for two time intervals: 0–0.6 Myr and 0.6–2.5 Ma. The central frequency and bandwidth for filtering analyses are 0.01 kyr^{-1} and 0.001305 kyr^{-1}.

1143 as much as ~1.2‰ occurred between ~2.5 and ~3.3 Ma. This relatively rapid increase in the benthic $\delta^{18}O$ within ~800 kyr indicates the onset of the Northern Hemisphere Glaciation (NHG). Prior to the onset, the light $\delta^{18}O$ with relatively small amplitudes depicts a warm climate during the late Pliocene. After the onset, the heavy $\delta^{18}O$ with increased amplitudes exhibits a process of strengthened NHG. This process has developed in step, with ~1.6 Ma and ~0.6 Ma as two important thresholds [*Berger and Jansen*, 1994]. Like the benthic $\delta^{18}O$, the chemical weathering intensity as recorded in K/Al and Ti/Al show continuously gradual increases and also similar amplitude variations after ~2.5 Ma (Figure 1).

[21] The global ice volume change as recorded in the benthic foraminiferal $\delta^{18}O$ is characterized by dominant 100 kyr cycles for the past 0.6 Myr, with the largest amplitudes occurring in the late Pleistocene [*Berger and Jansen*, 1994; *Wang et al.*, 2001]. Before ~0.6 Ma, the benthic foraminiferal $\delta^{18}O$ is characterized by dominant 41 kyr cycles with relatively small amplitudes. The transition of the dominant cycles in $\delta^{18}O$ from 41 kyr to 100 kyr is called the Mid-Pleistocene Revolution (MPR) event, which is the most prominent feature during the Pliocene and Pleistocene. The maximum entropy spectral analyses clearly demonstrate that the 100 kyr components in the $\delta^{18}O$ are weaker than the 41 kyr components between 0.6 and 2.5 Ma but much stronger after ~0.6 Ma (Figure 4a). The Gaussian band-pass filtering analysis also reveals that the largest amplitudes of the 100 kyr components of the $\delta^{18}O$ occur in the interval 0–0.6 Ma (Figure 4e).

[22] The Ti/Al record shows similar MPR event to that of the benthic foraminiferal $\delta^{18}O$, with the 41 kyr cycle being much stronger than the 100 kyr cycle prior to 0.6 Ma but much weaker after ~0.6 Ma (Figure 4b). The MPR event in the K/Al record is not as typical as that in the $\delta^{18}O$ and Ti/Al records. The spectrums in the chemical weathering intensity as recorded in the K/Al record and in the $\delta^{18}O$ show similarities but also differences. In the interval 0–0.6 Ma, the 100 kyr cycle of the K/Al is much stronger than the 41 kyr cycle, which is similar to that of the $\delta^{18}O$ and Ti/Al. But in the interval 0.6–2.5 Ma, the 100 kyr cycle in the K/Al is also stronger than the 41 kyr cycle, which is different from that of the $\delta^{18}O$ and Ti/Al (Figure 4c). Filtering analysis reveals significant 100 kyr cycles in the K/Al record in the interval 0–0.6 Ma but also evident 100 kyr cycles in the interval 0.6–4.5 Ma (Figure 4d). The 100 kyr cycle of the K/Al is consistently stronger than the 41 kyr cycle for the past 2.5 Myr, which implies consistent eccentricity forcing on the chemical weathering variability.

[23] Recognition of the MPR event in the K/Al and Ti/Al records reveals significant relationship between the NHG and the continental chemical weathering intensity in the East Asia. The consistently marked 100 kyr cycle in the K/Al record for the past 4 Myr indicate continuously strong eccentricity forcing on the chemical weathering change. The strong 100 kyr climate cycle in the late Pleistocene can be explained as a linear or nonlinear response to the late Pleistocene ice age [*Imbrie et al.*, 1993]. But, marked 100 kyr climate cycle in the early Pleistocene and the Pliocene is difficult to explain as a linear response because the 100 kyr ice age cycle is very weak during these periods. It is also beyond the ability of a linear version of the Milankovitch theory because the 100 kyr insolation cycle is much too small in amplitude and too late in phase to produce the corresponding climate cycle by directing forcing [*Imbrie et al.*, 1993]. It seems that besides the NHG forcing the eccentricity of the Earth's orbital geometry has played an important role in continuously modulating the regional climate in the East Asia.

4.1.2. Triggering of Chemical Weathering Strengthening by NHG

[24] How does the high latitude climate change like the fluctuation of the Northern Hemisphere ice sheet affect the chemical weathering in the Asian continent? The final onset of NHG at ~2.5 Ma ago is identified by increased amplitude of the benthic $\delta^{18}O$ of the Marine Isotope Stages (MISs) 100 and 99 (Figure 1a). Before ~2.5 Ma, glacials and interglacials are characterized by warm, wet climate and warmer, wetter climate respectively; after ~2.5 Ma, the Earth's climate

fluctuates between cold, dry glacials and warmer, moister interglacials [*Tian et al.*, 2002]. Corresponding to such a climate transition, the continental chemical weathering intensity as recorded in K/Al and Ti/Al keeps relatively constant in the long term changes prior to ~2.5 Ma but began to gradually increase after this time, with prolonged glacial/interglacial amplitudes (Figures 1b and 1c).

[25] Such a climate transition is also recorded in the regional SST (sea surface temperature) variations in the northern South China Sea. As indicated in the low resolution $U^{k'}_{37}$ SST records of ODP Site 1147/1148 from the northern South China Sea [*Jia et al.*, 2008], the SST is relatively stable prior to ~2.5 Ma ago but becomes rather variable with gradually increased amplitudes after ~2.5 Ma (Figure 4d). The U^{k}_{37} SST record at ODP Site 1143 from the southern South China Sea also indicates such a climate transition from equilibrium state to disequilibrium state (L. Li, personal communication, 2010). The published U^{k}_{37} and foraminiferal Mg/Ca SST records from different oceans which span the Pliocene and Pleistocene also record such a climate transition around the onset of NHG [*Lea et al.*, 2000; *Liu and Herbert*, 2004; *Wara et al.*, 2005; *de Garidel-Thoron et al.*, 2005; *Medina-Elizalde and Lea*, 2005; *Lawrence et al.*, 2006]. These SST records perform similar glacial/interglacial cycles during the Pliocene and the Pleistocene, and also record the MPR event which characterizes the global ice volume change.

[26] There probably exist some processes through atmosphere or ocean circulation which link the tropical SST with the high northern latitude climate. Green-house gases such as CO_2 probably act as the carrier of such processes through fluctuations in concentration [*Shackleton*, 2000]. The reconstructed CO_2 records from polar ice cores [*Petit et al.*, 1999; *Siegenthaler et al.*, 2005] or from boron isotopic composition of planktonic foraminiferal shells which records past seawater pH [*Hönisch et al.*, 2009] exhibit prominent glacial/interglacial cycles as seen in the global ice volume and tropical SST records. Interaction between the tropical SST and the high latitude climate is probably modulated by changes in the concentration of green-house gases such as CO_2 and water vapor [*Shackleton*, 2000]. The SST variability in the South China Sea and the Arabian Sea as well as the western Pacific and Indian Oceans determines the amount of latent heat transported by Asian summer monsoons from the oceans to the Asian continent. Releasing of the latent heat is finally achieved by precipitation on land. This logic seems to indicate that the Asian monsoon system is a major factor which affects the extent of the chemical weathering on the source regions. Relationship among erosion rate or chemical weathering, CO_2 concentration and long-term global cooling during the late Cenozoic is still ambiguous. *Raymo and Ruddiman* [1992] proposed a controversial hypothesis to depict the relationship. The uplift of the Tibetan Plateau and its positive feedbacks may have accelerated the chemical weathering which caused a drastic decline of atmospheric CO_2 concentration. The decrease of CO_2 concentration resulted in the global cooling in the Cenozoic, which led to the growth of large continental ice sheets in both hemispheres. But, this debatable hypothesis is challenged. For example, the most drastic decrease of the atmospheric CO_2 concentration happened during the Oligocene [*Pagani et al.*, 2005], but the occurrence of the most significant ice ages happened during the late Pliocene and the early Pleistocene. A lag of more than 10 Myr is very hard to understand. Our K/Al and Ti/Al as well as the benthic foraminiferal $\delta^{18}O$ records at ODP Site 1143 cannot clarify this relationship but provide some clues to uncover the interaction between the high latitude ice sheet development, the tropical SST and the tropical erosion rate or chemical weathering changes.

4.1.3. Variable Timing of Asian Summer Monsoon Due to NHG

4.1.3.1. Proxies of the East Asian Summer Monsoon and Its Variability Over the Past 5 Myr

[27] The idea of relating the chemical weathering to the Asian monsoon variability has been recently applied in two studies at ODP Site 1148 from the northern South China Sea [*Wei et al.*, 2006; *Clift et al.*, 2008]. The chemical weathering proxies at this site such as K/Al and C_{RAT} (Figure 2 and Supplementary Figure 4 of *Clift et al.* [2008]) have indicated a general pattern of the Asian summer monsoon variability on tectonic timescale during the Neogene.

[28] The magnetic susceptibility (MS) of the Quaternary loess-paleosol sequences and the underlain late Neogene Red Clay sequence from the Chinese Loess Plateau (CLP) has long been used as effective proxy of the East Asian summer monsoon variability [*Ding et al.*, 1999; *An et al.*, 2001]. A recent study in the loess-paleosol and Red Clay sequence in Lingtai has constructed a 7 Myr long MS record for the East Asia Summer monsoon variability [*Sun et al.*, 2010]. In the South China Sea a region which is greatly influenced by the East Asian summer and winter monsoons, a number of investigators have employed a series of records from the deep sea sediments as proxies of East Asian summer monsoon. These proxies include biogenic Ba [*Wehausen and Brumsack*, 2002] and opal [*Tian et al.*, 2005] which are related to paleoproductivity, $\delta^{18}O$ of seawater which indicates precipitation-related sea surface salinity [*Tian et al.*, 2006], and lithogenic accumulation which relates to riverine runoff [*Wehausen and Brumsack*, 2002]. As pointed out by *Clemens and Prell* [2003] and *Clemens et al.* [2008], no proxy currently in use in the South China Sea can claim a unique and direct response to East Asian summer and winter monsoons and all proxies have the potential to be modified by unrelated chemical, physical, or biological processes. For example, the influences from sea level change cannot be ignored in the South China Sea. Researchers have put forward a multiproxy frequency-specific approach which ignores the visual similarities in long-term trend among different monsoonal proxies but focuses on the common variance among different monsoon-influenced proxies at specific orbital frequency bands [*Clemens and Prell*, 2003; *Clemens et al.*, 2010]. This method stresses the similarity in the orbital spectrum among different monsoonal proxies and has been proved to be of great success in the study of the timing of the Asian monsoon variability relative to orbital and NHG forcing. Here we demonstrate that long-term changes in the mean and variance of certain records do reflect relevant and meaningful changes in monsoonal weathering.

[29] We compare records of K/Al of ODP Site 1143, K/Al and C_{RAT} of ODP Site 1148, K/Al and lithogenic flux and biogenic Ba flux of ODP Site 1146 and MS of the loess-paleosol as well as the Red Clay sequence in Lingtai (Figure 5). All the seven monsoonal proxy records show similar secular changes over the late Pliocene-Holocene

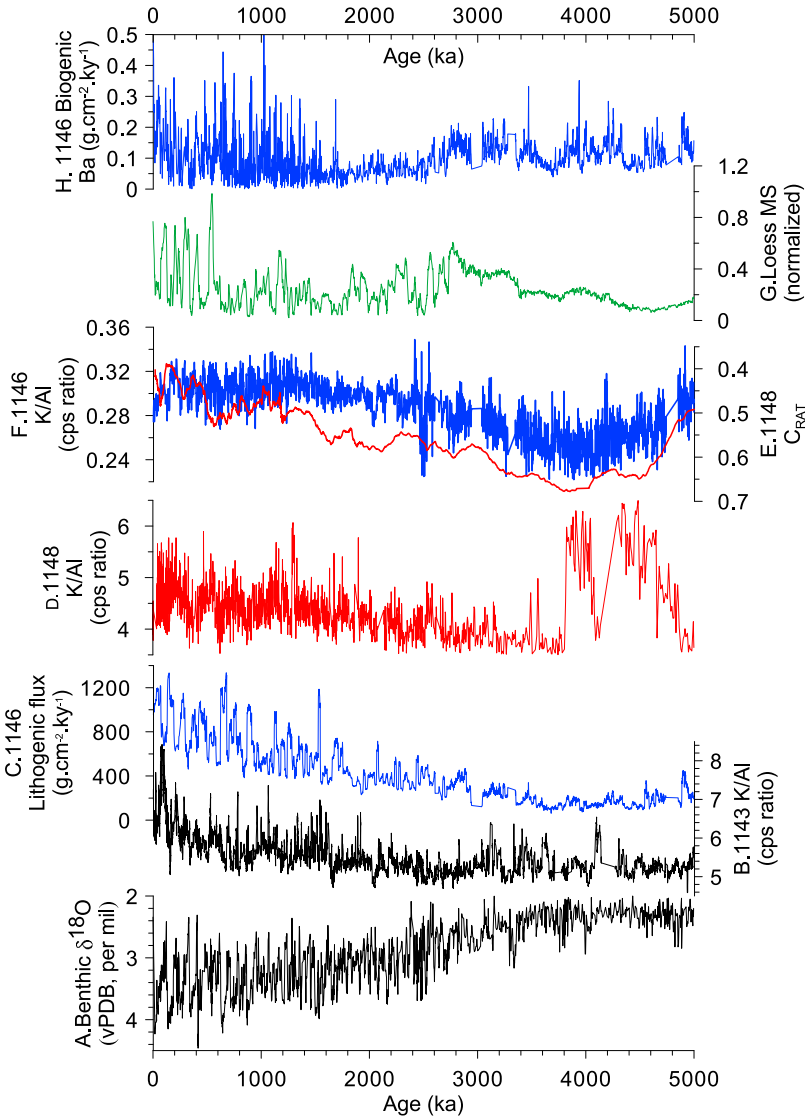

Figure 5. Climate records over the past 5 Myr. (a) benthic foraminiferal $\delta^{18}O$ of ODP Site 1143 [*Tian et al.*, 2002]; (b) K/Al (cps ratio) of ODP Site 1143; (c) lithogenic flux of ODP Site 1146 [*Clemens et al.*, 2008]; (d) K/Al (cps ratio) of ODP Site 1148 [*Clift et al.*, 2008]; (e) C_{RAT} of ODP Site 1148 [*Clift et al.*, 2008]; (f) K/Al (cps ratio) of ODP Site 1146 [*Clemens et al.*, 2008]; (g) magnetic susceptibility of the loess-paleosol and Red Clay sequences in Lingtai [*Sun et al.*, 2010]; (h) biogenic Ba of ODP Site 1146 in the northern South China Sea [*Clemens et al.*, 2008].

period. All the high resolution records except for the low resolution C_{RAT} record of ODP Site 1148 show augmented amplitude of the variability on glacial/interglacial cycle over the late Pleistocene, with high values during interglacials and low values during glacials. The K/Al records of ODP Sites 1148, 1146 and 1143 show different pattern before ~3.8 Ma but resemble one another after ~3.8 Ma (Figures 5b, 5d and 5f). The extreme high values of K/Al of ODP Site 1148 before ~3.8 Ma compared to that after this time and the sharp decrease from ~3.82 to ~3.8 Ma should not result from climate change but might be explained by changes in provenance of the deep sea sediments in the northern South China Sea. Similar high values is also observed in the K/Al records of ODP Site 1146 between 5 and 3.8 Ma (Figure 5f) [*Clemens et al.*, 2008], but it shows a gradual decrease during this period and then a gradual increase until the Holocene. Particularly, ODP Site 1146 K/Al record has a long-term trend that is so similar to that of the ODP Site 1148 C_{RAT} weathering record [*Clift et al.*, 2008], implying that both records are reliable indicators of chemical weathering, consistent across the Bay of Bengal and the South China Sea. The difference in the K/Al records between 5 and 3.8 Ma of the two adjacent ODP Sites in the northern South China Sea may be caused by ocean circulation change as that happened during the middle Miocene [*Tian et al.*, 2009] because ODP Site 1146 (water depth 2092 m) represents intermediate water and ODP Site 1148 (water depth 3294 m) represents deep water in the South China Sea.

[30] We also compared the spectral features of different monsoonal records. Spectral analyses (0–5 Ma) were per-

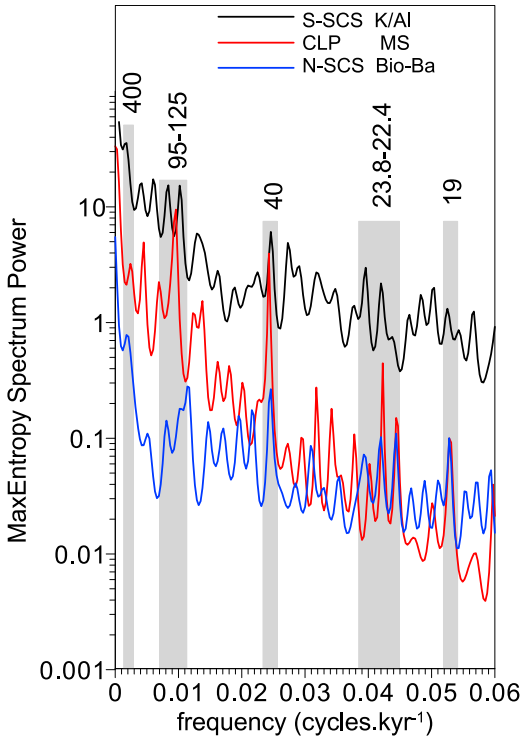

Figure 6. Spectrums of the records of K/Al (cps ratio) of ODP Site 1143 (black line), magnetic susceptibility of the loess-paleosol and Red Clay sequences in Lingtai (red line) [*Sun et al.*, 2010] and biogenic Ba of ODP Site 1146 in the northern South China Sea (blue line) [*Clemens et al.*, 2008]. Numbers denote the major orbital cycles, with unit of kyr.

formed on records of K/Al of ODP Site 1143, biogenic Ba flux of ODP Site 1146 and MS of the loess-paleosol and the Red Clay sequence in Lingtai (Figure 6). The spectrums of the three records show similar features at the primary orbital frequencies, that all have prominent long eccentricity cycle (400 kyr), two marked eccentricity cycles (95–125 kyr), one prominent obliquity cycle (40 kyr) and several precession cycles (19 kyr, 22.4–23.8 kyr).

[31] The above comparisons indicate that K/Al and Ti/Al of ODP Site 1143 are reliable proxies which record orbital scale variability of the East Asian summer monsoon over the late Pliocene and Pleistocene period. Other processes such as provenance and probable ocean circulation changes should also have impacts on the K/Al and Ti/Al variations of ODP Site 1143. However, as indicated in a study of Asian monsoon variability by a multiproxy approach [*Clemens et al.*, 2008], the monsoonal variability at specific orbital frequency can be revealed in the K/Al or Ti/Al records of ODP Site 1143.

[32] The generally secular pattern of all the monsoonal proxy records (Figure 5) indicate the late Pliocene-Holocene intensification of the East Asian summer monsoon, which is corroborated by the other East Asian summer monsoon records [*An et al.*, 2001; *Tian et al.*, 2004, 2006; *Zheng et al.*, 2004]. As evidenced in the K/Al and Ti/Al records of ODP Site 1143 (Figure 1), the marked strengthening of the East Asian summer monsoon commenced at ~2.5 Ma which agrees well with that evidenced in the loess-paleosol sequences [*An et al.*, 2001]. In most cases, the East Asian summer monsoon is consistently stronger during interglacials than during glacials and the glacial summer monsoon has gradually strengthened since ~2.5 Ma. The monsoonal fluctuations exhibit the largest amplitudes during the late Pleistocene, showing strong 100 kyr cycles as that in the global ice volume change.

4.1.3.2. Nonstationary Phase of East Asian Summer Monsoon Relative to NHG Forcing

[33] A previous study based on sea surface salinity reconstruction at Site 1143 reveals s linear response of the East Asian summer monsoon variability to the onset of NHG during the late Pliocene period, but with much bigger phase lagged at the 41-kyr and 23-kyr bands than in the Pleistocene [*Tian et al.*, 2006]. As revealed in a study from the Arabian Sea, the South Asian summer monsoon (Indian Ocean summer monsoon) is sensitive to the extent of the NHG at the 41-kyr and 23-kyr bands [*Clemens et al.*, 1996]. Over the past 2.6 Myr, the phase (timing) of strong South Asian summer monsoon has changes by ~83° at the 23-kyr band and ~124° at the 41-kyr band relative to the phase of maximum global ice volume [*Clemens et al.*, 1996]. We computed evolutive phases of the maximum K/Al relative to the maximum benthic foraminiferal $\delta^{18}O$ for the past 5 Myr (Figures 7a and 7b). At the 41 kyr (obliquity) band, the negative phases from ~4 Ma to ~2.75 Ma indicate a lag of the maximum global ice volume relative to the maximum East Asian summer monsoon strength, whereas the positive phases after ~2.75 Ma imply a lead relationship. A marked phase jump from −60° to 120° occurs at ~2.75 Ma, being nearly synchronous with the onset of the NHG. This 180° phase shift was also discovered between the East Asian summer and winter monsoons at both the obliquity and the precession bands at ~2.75 Ma [*Clemens et al.*, 2008; *Sun et al.*, 2010]. Before ~2.75 Ma, the East Asian summer and winter monsoons coupled each other but after ~2.75 Ma they drifted apart from each other. The phase of strong winter monsoons shifted toward ice maxima and the phase of strong summer monsoons shifted toward ice minima, reflecting the combined influence of fast physics variables (latent and sensible heating) and slow physics variables (glacial boundary conditions) [*Clemens et al.*, 2008]. The shift from Southern Hemisphere ice volume dominance during the Pliocene to Northern Hemisphere ice volume dominance during the Pleistocene just occurred at ~2.75 Ma and caused this 180° phase shift between the Asian summer and winter monsoons. This interpretation stresses the great influences of the global ice volume change on the Asian monsoon evolution.

[34] A marked phase shift at the obliquity band is also observed at ~1.85 Ma, which seems to correspond to the phase shift at the precession band starting earlier at ~2.1 Ma. The phase shift at the obliquity band shows an increasing trend whereas that at the precession band exhibits a decreasing trend. These phase shifts are not consistent with any marked event in the global ice volume record. Similar phase shifts at the obliquity and the precession band are also found in the response of the South Asian summer monsoon to global ice volume change at ~1.7 Ma, which was interpreted to be related to large scale changes in African vegetation and meteoric waters as well as African aridity [*Clemens et al.*,

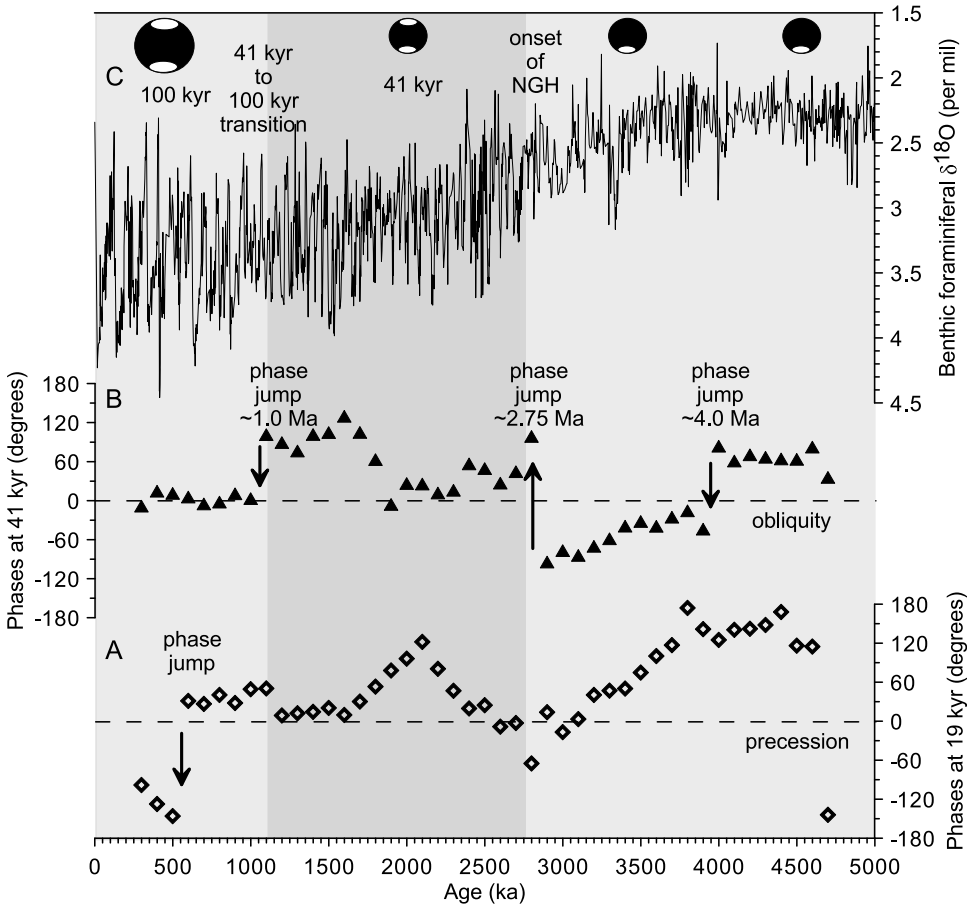

Figure 7. Phase evolution at (a) the precession and 9b) the obliquity bands. The phases are calculated by evolutive cross BTukey spectral analyses of K/Al (cps ratio) with (c) benthic foraminiferal δ^{18}O at ODP Site 1143 over the past 5 Myr. We use a 500-kyr window and a moving step of 100 kyr. The arrows indicate phase jumps. BTukey spectrum uses a Bartlett window with a bandwidth of 0.00234448 kyr^{-1}.

1996]. The African influences seem to be too far away from the South China Sea to affect the regional East Asian summer monsoon, but the tropical climate system in East Asia such as the regional hydrology should have the potentiality to alter the ocean-atmosphere circulation and finally affect the East Asian summer monsoon.

[35] The other phase jump occurs at ~1.1 Ma, which is consistent with the early onset of the so-called Croll period [*Berger and Jansen*, 1994] or the early transition of the so-called MPR (middle Pleistocene Revolution). The phase at the 19 kyr band gradually decreases from ~4 Ma to ~2.75 Ma, displaying a similar trend as in the phase at the 41 kyr band. But at ~2.75 Ma, no rapid jump in the phase at the 19 kyr band occurs but a gradual increase until ~2.1 Ma and then a gradual decrease until ~1.1 Ma. The phase at the 19 kyr band only jumps at ~0.6 Ma, following the beginning of the so-called Milankovitch period [*Berger and Jansen*, 1994] or the commencement of the late Pleistocene ice age characterized by dominant 100 kyr climate cycles (Figure 7a). The above evidences support nonstationary phases of East Asian summer monsoon variations relative to the NHG during the late Pliocene and the Pleistocene, and also highlight great influences from the NHG on the East Asian summer monsoon evolution.

4.2. Truncated-Insolation Forcing on the Long Eccentricity (400 kyr) Cycles in Chemical Weathering

[36] The K/Al and the benthic foraminiferal δ^{18}O records at Site 1143 demonstrate standard precession (19 kyr, 23 kyr), obliquity (40 kyr) and eccentricity (95–125 kyr) cycles (Figures 8a and 8b) over the interval 0–5 Ma as shown in the orbital forcing (ETP) (Figure 8a). Cross spectral analyses also reveal highly coherent relationship of the elemental records with the ETP and the δ^{18}O at these basic orbital cycles (Figure 8). Of the most interest in the spectrums of the elemental records is that the K/Al performs a prominent 400 kyr cycle as the ETP and it is highly coherent with the ETP at the 400 kyr long eccentricity cycle (Figure 8a). The evolutive spectral analyses reveal uninterrupted strong 400 kyr cycles in both the ETP and the K/Al and Ti/Al records over the past 5 Myr (Figures 9b, 9c, and 9d), but not in the benthic foraminiferal δ^{18}O records (Figure 9a). The uninterrupted strong 400 kyr cycles seem to be the unique features of the chemical weathering or the monsoonal records (K/Al and Ti/Al) which are not possessed by global ice volume (δ^{18}O) records.

[37] The amplitude variation of the Earth's eccentricity has a dominant cycle of ~400 kyr over the past 25 Myr [*Laskar et al.*, 2004]. Even the monthly mean insolation at

65°N shows high sensitivity to variations at the 400 kyr band over the past 23 Myr as proved by f-test evaluation, though the spectral density at this band is rather small relative to that at the dominant 21 kyr and 41 kyr cycles of the insolation [*Tian et al.*, 2008]. Prominent 400 kyr cycle has been prevalent in the Oligocene and the early Miocene climate records and these climate cycles are highly coherent with the orbital forcing [*Zachos et al.*, 2001; *Wade and Pälike*, 2004; *Pälike et al.*, 2006]. But, with the growing of the Antarctic and the Northern Hemisphere ice sheets, the 400 kyr climate cycle has been absent or obscured during the late Pliocene and the Pleistocene periods [*Wang et al.*, 2010]. The spectrum of the benthic foraminiferal δ^{18}O averaged over the past 5 Myr reveals the absence of the 400 kyr cycle in global ice volume change [*Wang et al.*, 2004, Figure 3]. This is the so-called "400-kyr problem" [*Imbrie and Imbrie*, 1980]. Furthermore, the 400 kyr cycle of the ocean carbon reservoir is greatly obscured in the late Pleistocene as evidenced by a significant ~500 kyr cycle in the spectrums of the global benthic foraminiferal δ^{13}C [*Wang et al.*, 2004, 2010]. The late Pleistocene ice age seems to play a major role in obscuring the long eccentricity cycle in the climate responses.

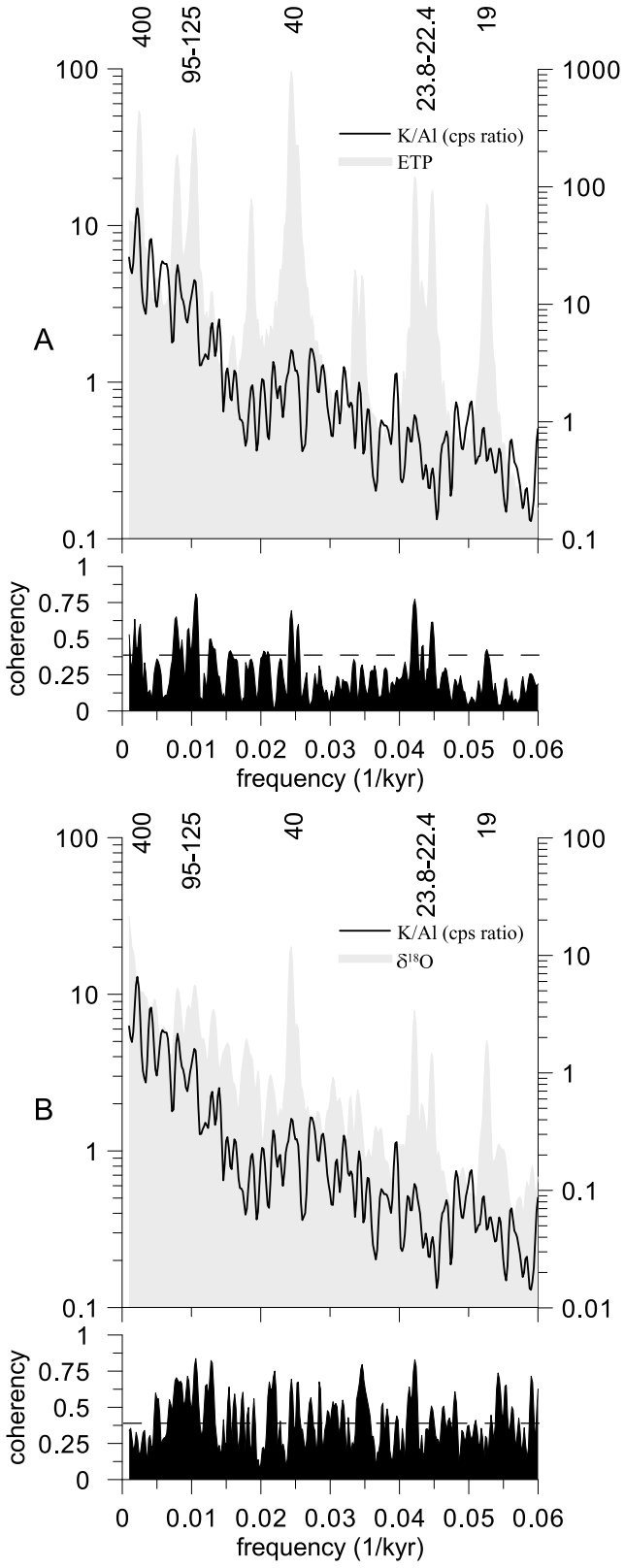

[38] Besides our K/Al and Ti/Ai records, the African monsoon proxy records from the Mediterranean Sea also perform uninterrupted strong 400 kyr cycle over the past 5 Myr. As displayed in the cross spectral analyses of the MEDSTACK (Mediterranean stack δ^{18}O and δ^{13}C, proxies of African monsoon [*Wang et al.*, 2010]) records with the ETP, the Mediterranean isotopic records show prominent 400 kyr cycles in the spectrum averaged over the interval 0–5 Ma and are also highly coherent with the ETP at this band [from *Wang et al.*, 2010, Figure 2b]. The other Asian summer monsoon proxy records such as the MS of the loess-paleosol sequence in Lingtai and the Biogenic Ba flux of ODP Site 1146 in the northern South China Sea also perform significant 400 kyr long eccentricity cycles over the past 5 Myr as revealed in the K/Al and Ti/Al records at ODP Site 1143 (Figure 6). Summarizing the above spectral evidences, the 400 kyr long eccentricity cycle is a specific feature possessed by the Asian and African monsoon systems at least for the past 5 Myr. Although the monsoonal variability has been closely related to the NHG during the Pliocene and the Pleistocene, as seen in the K/Al and Ti/Al as well as other monsoonal records, the 400 kyr cycle of the monsoonal variability has not been obscured by the late Pleistocene ice ages.

[39] In a linear version of the Milankovitch theory, The Earth's orbital parameters control the seasonal and latitudinal changes of insolation which finally controls the climate change on The Earth. However, a direct insolation forcing cannot produce a marked 400 kyr cycle in the monsoonal response because the eccentricity's contribution to insolation

Figure 8. Cross BTukey spectral analyses of K/Al (cps ratio) with (a) ETP (0–5 Ma) and (b) benthic foraminiferal δ^{18}O (0–5 Ma). The K/Al ratio and δ^{18}O are from ODP Site 1143. ETP refers to the sum of the normalized eccentricity (multiplied by −1), obliquity (multiplied by −1) and climatic precession (multiplied by 0.5) time series derived from the La2004 solution [*Laskar et al.*, 2004]. BTukey spectrum uses a Bartlett window with a bandwidth of 0.00234448 kyr^{-1}. Nonzero coherence is higher than 0.384464. The error estimation on the power spectrum is between 0.625486 and 2.05554. Numbers denote the major orbital cycles, with unit of kyr.

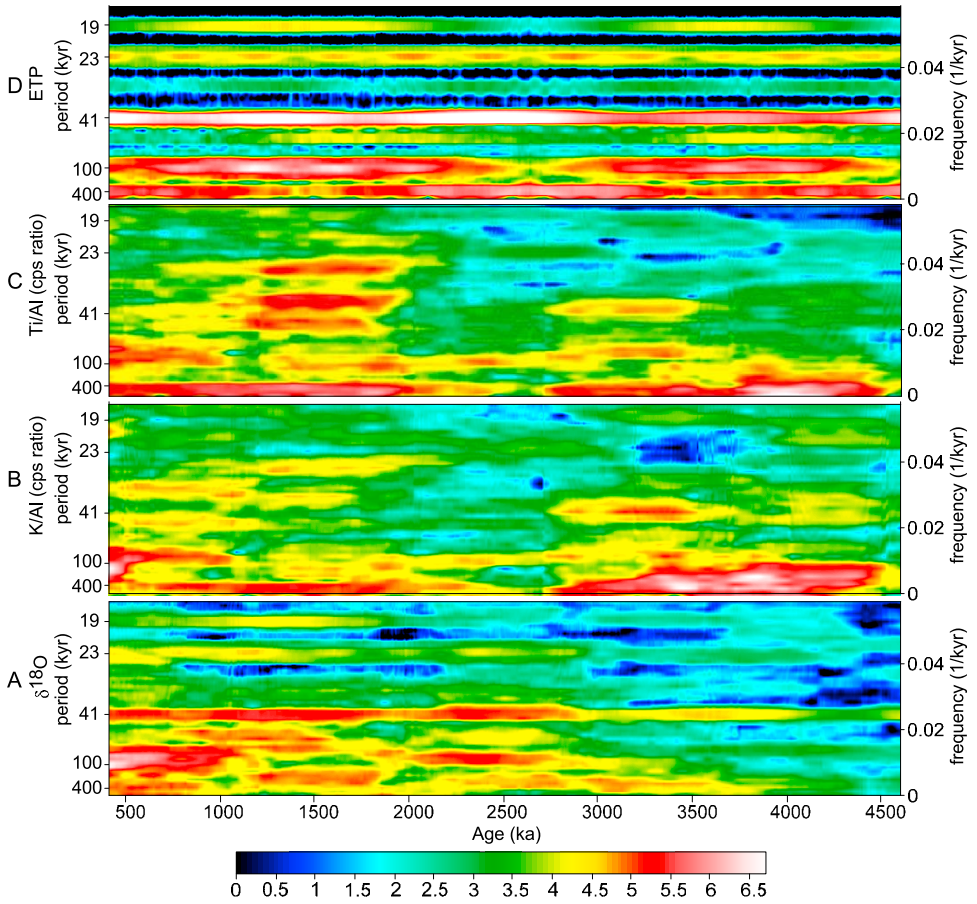

Figure 9. Evolutive spectrums over the past 5 Myr on (a) benthic foraminiferal $\delta^{18}O$ at Site 1143, (b) K/Al (cps ratio) at Site 1143, (c) Ti/Al (cps ratio) at Site 1143, and (d) ETP. ETP refers to the sum of the normalized eccentricity (multiplied by −1), obliquity (multiplied by −1) and climatic precession (multiplied by 0.5) time series derived from the La2004 solution [*Laskar et al.*, 2004]. Parameter setting of evolutive spectrum is p = 2, k = 3, taper length is 819.2 ka, and time step is 5 kyr. Indication of the parameters for evolutive spectral analyses is given by *Ma et al.* [2010]. The color bar is of the evolutive spectrum which indicates the spectral density.

is too small (<0.1%) to effect climate change [*Imbrie et al.*, 1993]. But in theory, fluctuation of the eccentricity which controls insolation by amplitude modulation on the precession should be the original source of the 400 kyr cycle in the monsoonal records. If we calculate the average spectrum of the benthic foraminiferal $\delta^{18}O$ between 1.2 Ma and 5.2 Ma without considering the late Pleistocene, we can find a 400 kyr cycle in the spectrum which stands in parallel with three other non-orbital cycles [*Clemens and Tiedemann*, 1997, Figure 2]. Although this 400 kyr cycle is much weaker than the 41 kyr and 21 kyr cycles, it is highly coherent with the marked 400 kyr cycle of the truncated insolation (July 65°N) over the interval 1.2–5.2 Ma [*Clemens and Tiedemann*, 1997]. Therefore, the 400 kyr cycles in global ice volume change during the late Pliocene and the early Pleistocene probably originate through an asymmetrical response mechanism that preferentially introduces variance into the climate system from the warmer portions of the eccentricity-modulated precession cycle [*Clemens and Tiedemann*, 1997].

[40] The 400 kyr cycle in the Asian monsoon system probably also originates from such an asymmetrical response mechanism like that of the 400 kyr cycle in the Pliocene and early Pleistocene global ice volume change. Usually, the magnitude of precipitation is positively correlated with the intensity of the summer monsoon. The latent heat transferred from ocean to atmosphere relies on evaporation and finally determines the magnitude of precipitation. Theoretically, evaporation increases with temperature, but this condition rarely occurs naturally. In contrast, on a global basis, the latent heat is negatively correlated with temperature. Modern observations on seasonal and interannual timescales reveal that strong winds in the winter hemisphere usually correspond to increased latent heat and decreased SST. Latent heat maxima and monsoon maxima should be associated with Southern Hemisphere winters characterized by strong atmospheric circulation [*Clemens and Tiedemann*, 1997]. In both hemispheres, winter SST corresponds to low insolation of a year. On orbital time scale, the monsoon maxima might preferentially respond to the lower portions of the insolation of which the amplitude is controlled by the eccentricity-modulated precession cycle. As revealed in the cross spectrum over the interval 0–5 Ma, the truncated insolation (low values of 65°N insolation was truncated) and the K/Al are

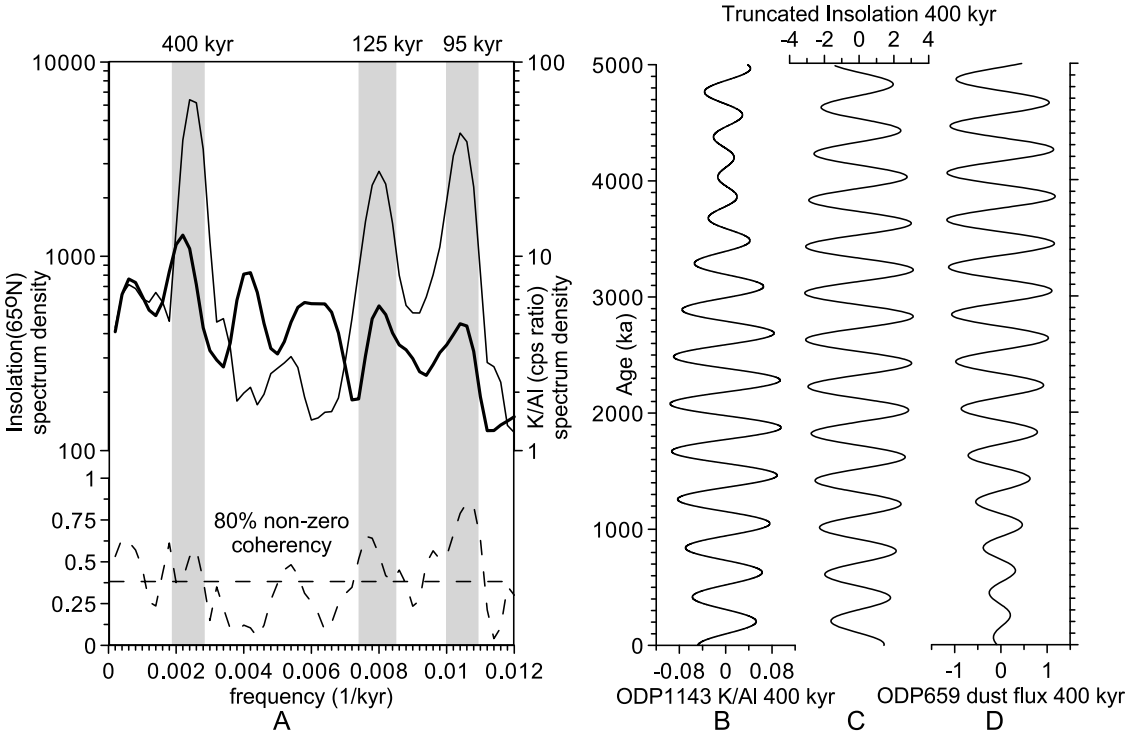

Figure 10. (a) Cross BTukey spectral analyses of K/Al (cps ratio) with the truncated insolation at 65°N (0–5 Ma), and 400 kyr Gauss band-pass filtering analyses on (b) K/Al ratio, (c) truncated insolation, and (d) the dust flux of ODP Site 659 [*Tiedemann et al.*, 1994]. BTukey spectrum uses a Bartlett window with a bandwidth of 0.00234448 kyr^{-1}. Cross BTukey spectrum using a Bartlett window with a bandwidth of 0.00100254. Nonzero coherence is higher than 0.38444. The error estimation on the power spectrum is between 0.625503 and 2.05541. The central frequency and bandwidth for Gauss band-pass filtering analyses are 0.0025 kyr^{-1} and 0.0002 kyr^{-1}, respectively.

highly coherent at the short eccentricity cycles (95 kyr and 125 kyr) and the long eccentricity cycle (400 kyr) (Figure 10a). The 400 kyr components of the truncated insolation and K/Al records are nearly anti-correlated to each other over the past 5 Myr, with insolation minimum (low winter hemisphere SST) corresponding to K/Al maxima or monsoon maxima (Figure 10b). The dust flux of ODP Site 659 from the northern Atlantic [*Tiedemann et al.*, 1994] records the African monsoon variability, and also displays uninterrupted 400 kyr long eccentricity cycles over the

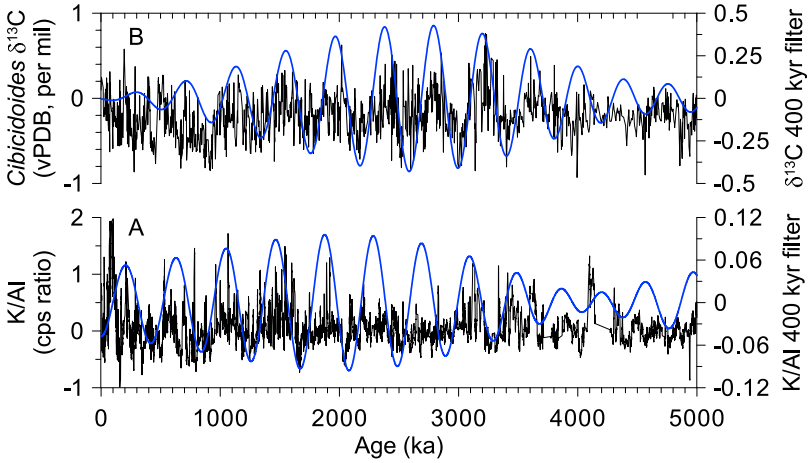

Figure 11. (a) K/Al (cps ratio) of ODP Site 1143 (0–5 Ma) and (b) *Cibicidoides* $\delta^{13}C$ of ODP Site 1143 (0–5 Ma). K/Al was detrended by a locally weighted (30%) fit (least squares error) to remove the long-term trend. Blue lines denote the 400 kyr cycles of each record which were obtained by Gauss band-pass filtering, with central frequency of 0.0025 $kyr^{-1}$and bandwidth of 0.0002 kyr^{-1}.

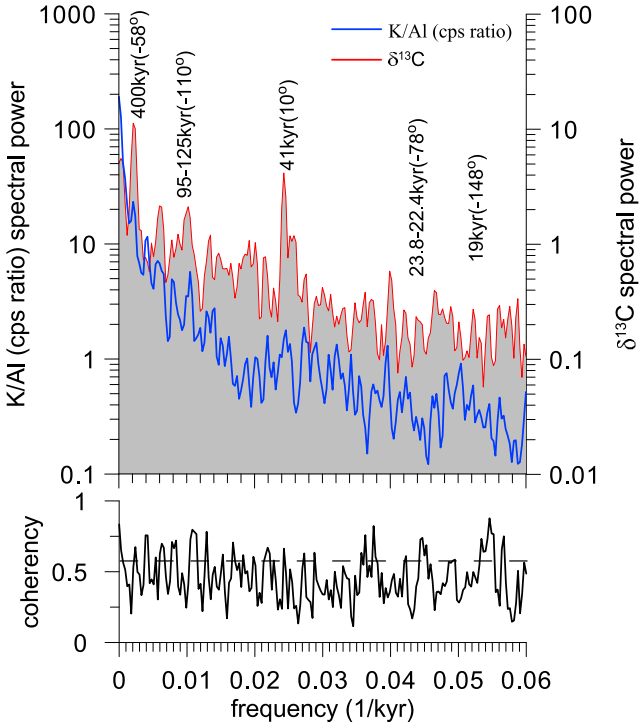

Figure 12. Cross BTukey spectral analyses of K/Al (cps ratio) with the benthic foraminiferal δ^{13}C (0–5 Ma). BTukey spectrum uses a Bartlett window with a bandwidth of 0.000664717 kyr^{-1}. Nonzero coherence is higher than 0.459231. The error estimation on the power spectrum is between 0.576555 and 2.54441.

past 5 Myr [*Wang et al.*, 2010] which are anti-correlated to the 400 kyr components of the truncated insolation (Figure 10b).

4.3. Relationship of Chemical Weathering With Ocean Carbon Reservoir on Orbital Timescale

[41] The Uplift-Weathering Hypothesis [*Raymo and Ruddiman*, 1992] proposed that tectonically driven increases in chemical weathering may have resulted in a decrease of atmospheric CO_2 concentration over the past 40 Myr The ocean reservoir contains most of the carbon in the global carbon budget. Qualitative or quantitative analysis of the relationship between chemical weathering and ocean carbon reservoir is of great help in the study of global carbon cycle. A completely compiled low resolution bulk carbonate δ^{13}C record of the deep sea sediments shows a decrease in δ^{13}C during the late Cenozoic, which was interpreted as a drop of the buried organic carbon in the ocean rather than carbonate from 20% to 10% over the course of the Neogene causing a net addition of CO_2 to the atmosphere [*Shackleton*, 1987]. Just during this period, the oceanic ^{87}Sr/^{86}Sr ratio recorded by marine carbonates has increased, showing an opposite trend to that of the bulk carbonate δ^{13}C. This pronounced increase in the late Cenozoic oceanic ^{87}Sr/^{86}Sr is widely explained by a considerable increase in the delivery of radiogenic strontium from land which could have been caused by increases in global chemical weathering rates [*Raymo and Ruddiman*, 1992]. On tectonic timescale, in brief, variability of ocean carbon reservoir or global carbon cycle is largely related to changes in chemical weathering rate.

[42] The fairly high resolution K/Al and benthic foraminiferal δ^{13}C records of ODP Site 1143 provide a chance to probe the relationship of chemical weathering with ocean carbon reservoir over the past 5 Myr on orbital timescale, for example the coherence between their variability on the specific orbital frequencies. The K/Al and δ^{13}C records are from the same site, along with the meters composite depth profile and owning the same age model [*Tian et al.*, 2002]. Both records perform similar glacial/interglacial cycles over the time interval 0–5 Ma, with high values during interglacials indicating intensified chemical weathering and high CO_2 concentration in the atmosphere and low values during glacials implying weakened chemical weathering and low CO_2 concentration (Figure 11). Of the particular interest are the prominent 400 kyr long eccentricity cycles which consistently exist in both K/Al and δ^{13}C records over the past 5 Myr, as highlighted by Gauss band-pass filter (Figure 11). The cross spectral analysis confirms the prominent 400 kyr cycle in the both records, and also reveals the marked 100 kyr short eccentricity cycles, the 41 kyr obliquity cycles and 19–23 kyr precession cycles in the K/Al and δ^{13}C records (Figure 12). Additionally, both the K/Al and the δ^{13}C records are highly coherent with each other at all these orbital frequencies (Figure 12). The K/Al maximum lags (leads) the δ^{13}C maximum (minimum) at the eccentricity (400 kyr, 95–125 kyr) and the precession bands (19 kyr, 22–24 kyr) (Figure 12). The K/Al maximum is nearly synchronous with the δ^{13}C maximum at the obliquity band (41 kyr) if considering the phase errors (Figure 12). The phase relationship reveals the timing of the chemical weathering variability relative to ocean carbon reservoir change on the specific orbital frequencies, that an increase of the chemical weathering rate causes a decrease in organic carbon burial and an enrichment of the seawater ^{12}C and therefore a decrease of the oceanic δ^{13}C which should result in a net addition of CO_2 to the atmosphere. Probably, this phase relationship between chemical weathering process and ocean carbon isotopes can be tentatively taken into account when simulating global carbon cycle by a box model approach [*Walker and Kasting*, 1992; *Pälike et al.*, 2006; *Merico et al.*, 2008].

5. Conclusion

[43] The K/Al and Ti/Al records at ODP Site 1143 which are obtained by nondestructive X-ray fluorescence (XRF) core scanning have documented the Asian chemical weathering and summer monsoon history over the past 5 Myr. Corresponding to the onset of the NHG, the chemical weathering and the East Asian summer monsoon begin to markedly intensify from ~2.5 Ma. Under the great influences from the NHG, the East Asian summer monsoon has exhibited non-stationary phases relative to the global ice volume change at the obliquity and the precession bands over the past 5 Myr. Besides regular glacial/interglacial cycles like that in the benthic foraminiferal δ^{18}O, the chemical weathering and the East Asian summer monsoon display strong 400 kyr and 100 kyr cycles over the past 5 Myr. Particularly, these cycles are highly coherent with the long and short eccentricity cycles in the truncated insolation at 65°N, respectively. We conclude that besides the NHG the

eccentricity has played a great role in modulating the chemical weathering and monsoon evolution during the late Pliocene and the Pleistocene. Cross spectral analysis between the K/Al and benthic foraminiferal $\delta^{13}C$ records of ODP Site 1143 also reveals highly coherent relationship between changes in the chemical weathering intensity and ocean carbon reservoir at the eccentricity, obliquity and precession bands during the late Pliocene and Pleistocene. This probably indicate that on orbital timescale an increase in chemical weathering rate may result in a decrease in oceanic $\delta^{13}C$ and a net addition of CO_2 to the atmosphere.

[44] **Acknowledgments.** This research used samples provided by the Integrated Ocean Drilling Program (IODP). We thank Lallan Gupta and Toshio Hisamitsu for help on transporting cores to Tongji University for scanning. Funding for this research was provided by the NSFC (grant 40776028, grant 40976024), the NKBRSF (grant 2007CB815902) and the FANEDD (grant 2005036) and the State Key Laboratory of Marine Geology, Tongji University (grant MG20080201). This research was also sponsored by Shanghai Rising-Star Program (grant 10QH1402600), Fok Ying Tong Education Foundation (111016) and program for New Century Excellent Talents in University (NCET-08-0401).

References

An, Z. S., J. E. Kutzbach, W. L. Prell, and S. Porter (2001), Evolution of Asian monsoons and phased uplift of the Himalaya-Tibetan Plateau since late Miocene times, *Nature*, *411*, 62–66, doi:10.1038/35075035.

Berger, W. H., and E. Jansen (1994), Mid-Pleistocene climate shift: The Nansen connection, in *The Polar Oceans and Their Role in Shaping the Global Environment*, *Geophys. Monogr. Ser.*, vol. 84, edited by O. M. Johannessen, R. D. Muench, and J. E. Overland, pp. 295–311, AGU, Washington, D. C.

Boyle, E. A. (1983), Chemical accumulation variations under the Peru Current during the past 130,000 years, *J. Geophys. Res.*, *88*, 7667–7680, doi:10.1029/JC088iC12p07667.

Clemens, S. C., and W. L. Prell (2003), A 350,000 year summer-monsoon multi-proxy stack from the Owen Ridge, northern Arabian Sea, *Mar. Geol.*, *201*(1–3), 35–51, doi:10.1016/S0025-3227(03)00207-X.

Clemens, S. C., and R. Tiedemann (1997), Eccentricity forcing of Pliocene–early Pleistocene climate revealed in a marine oxygen-isotope record, *Nature*, *385*, 801–804, doi:10.1038/385801a0.

Clemens, S. C., et al. (1996), Nonstationary phase of the Plio-Pleistocene Asian monsoon, *Science*, *274*, 943–948, doi:10.1126/science.274.5289.943.

Clemens, S. C., W. L. Prell, Y. Sun, Z. Liu, and G. Chen (2008), Southern Hemisphere forcing of Pliocene $\delta^{18}O$ and the evolution of Indo-Asian monsoons, *Paleoceanography*, *23*, PA4210, doi:10.1029/2008PA001638.

Clemens, S. C., W. L. Prell, and Y. Sun (2010), Orbital-scale timing and mechanisms driving Late Pleistocene Indo-Asian summer monsoons: Reinterpreting cave speleothem $\delta^{18}O$, *Paleoceanography*, *25*, PA4207, doi:10.1029/2010PA001926.

Clift, P. D., K. Hodges, D. Heslop, R. Hannigan, L. V. Hoang, and G. Calves (2008), Correlation of Himalayan exhumation rates and Asian monsoon intensity, *Nat. Geosci.*, *1*, 875–880, doi:10.1038/ngeo351.

de Garidel-Thoron, T., Y. Rosenthal, F. Bassinot, and L. Beaufort (2005), Stable sea surface temperatures in the western Pacific warm pool over the past 1.75 million years, *Nature*, *433*, 294–298, doi:10.1038/nature03189.

Ding, Z. L., S. F. Xiong, J. M. Sun, S. L. Yang, Z. Y. Gu, and T. S. Liu (1999), Pedostratigraphy and paleomagnetism of a 7.0 Ma Eolian loess–Red Clay sequences at Lingtai, Loess Plateau, north-central China and implications for paleomonsoon evolution, *Palaeogeogr. Palaeoclimatol. Palaeoecol.*, *152*, 49–66, doi:10.1016/S0031-0182(99)00034-6.

Grothmann, A. (1996), Rezente Verbreitungsmuster vulkanischer,terrigener und biogener Komponenten und stabiler Kohlen stoff- und Sauerstoff-Isotope in Sedimenten der Südchina-See, M.Sc. thesis, Kiel Univ., Kiel, Germany.

Haug, G. H., and R. Tiedemann (1998), Effect of the formation of the Isthmus of Panama on Atlantic Ocean thermohaline circulation, *Nature*, *393*, 673–676, doi:10.1038/31447.

Haug, G. H., D. M. Sigman, R. Tiedemann, T. F. Pedersen, and M. Sarnthein (1999), Onset of permanent stratification in the subarctic Pacific Ocean, *Nature*, *401*, 779–782, doi:10.1038/44550.

Hönisch, B., N. G. Hemming, D. Archer, M. Siddall, and J. F. McManus (2009), Atmospheric carbon dioxide concentration across the Mid-Pleistocene Transition, *Science*, *324*, 1551–1554, doi:10.1126/science.1171477.

Imbrie, J., and J. Z. Imbrie (1980), Modeling the climatic response to orbital variations, *Science*, *207*, 943–953, doi:10.1126/science.207.4434.943.

Imbrie, J., et al. (1993), On the structure and origin of major glaciation cycles: 2. The 100,000-year cycle, *Paleoceanography*, *8*, 699–735, doi:10.1029/93PA02751.

Jansen, J. H. F., et al. (1998), CORTEX, a shipboard XRF scanner for element analyses in split sediment cores, *Mar. Geol.*, *151*, 143–153, doi:10.1016/S0025-3227(98)00074-7.

Jia, G., F. Chen, and P. Peng (2008), Sea surface temperature differences between the western equatorial Pacific and northern South China Sea since the Pliocene and their paleoclimatic implications, *Geophys. Res. Lett.*, *35*, L18609, doi:10.1029/2008GL034792.

Koopmann, B. (1981), Saharan dust deposition in the subtropical Atlantic during the last 25,000 years (in German), *Meteor Forschungsergeb., Reihe C*, *5*, 23–54.

Kump, L. R., S. L. Brantley, and M. A. Arthur (2000), Chemical weathering, atmospheric CO_2, and climate, *Annu. Rev. Earth Planet. Sci.*, *28*, 611–667, doi:10.1146/annurev.earth.28.1.611.

Laskar, J., F. Joutel, and F. Boudin (1993), Orbital, precessional, and insolation quantities for the Earth from 220 Myr to 110 Myr, *Astron. Astrophys.*, *270*, 522–533.

Laskar, J., P. Robutel, F. Joutel, M. Gastineau, A. C. M. Correia, and B. Levrard (2004), A long term numerical solution for the insolation quantities of the Earth, *Astron. Astrophys.*, *428*, 261–285, doi:10.1051/0004-6361:20041335.

Lawrence, K. T., Z. Liu, and T. D. Herbert (2006), Evolution of the eastern tropical Pacific through Plio-Pleistocene glaciation, *Science*, *312*, 79–83, doi:10.1126/science.1120395.

Lea, D. W., D. K. Pak, and H. J. Spero (2000), Climate impact of late Quaternary equatorial Pacific sea surface temperature variations, *Science*, *289*, 1719–1724, doi:10.1126/science.289.5485.1719.

Liu, Z., and T. D. Herbert (2004), High-latitude influence on the eastern equatorial Pacific climate in the early Pleistocene epoch, *Nature*, *427*, 720–723, doi:10.1038/nature02338.

Liu, Z., A. Trentesaux, S. C. Clemens, C. Colin, P. X. Wang, B. Q. Huang, and S. Boulay (2003), Clay mineral assemblages in the northern South China Sea: Implications for East Asian monsoon evolution over the past 2 million years, *Mar. Geol.*, *201*, 133–146, doi:10.1016/S0025-3227(03)00213-5.

Liu, Z., C. Colin, W. Huang, K. P. Le, S. Tong, Z. Chen, and A. Trentesaux (2007), Climatic and tectonic controls on weathering in south China and Indochina Peninsula: Clay mineralogical and geochemical investigations from the Pearl, Red, and Mekong drainage basins, *Geochem. Geophys. Geosyst.*, *8*, Q05005, doi:10.1029/2006GC001490.

Ma, W., J. Tian, and Q. Li (2010), Astronomically modulated late Pliocene equatorial Pacific climate transition and Northern Hemisphere ice sheet expansion, *Chin. Sci. Bull.*, *55*(2), 212–220, doi:10.1007/s11434-009-0310-4.

Martinez, N. C., R. W. Murray, R. C. Thunell, L. C. Peterson, F. Muller-Karger, Y. Astor, and R. Varela (2007), Modern climate forcing of terrigenous deposition in the tropics (Cariaco Basin, Venezuela), *Earth Planet. Sci. Lett.*, *264*, 438–451, doi:10.1016/j.epsl.2007.10.002.

Martinez, N. C., R. W. Murray, G. R. Dickens, and M. Kolling (2009), Discrimination of sources of terrigenous sediment deposited to the Central Arctic Ocean through the Cenozoic, *Paleoceanography*, *24*, PA1210, doi:10.1029/2007PA001567.

Martinez, N. C., R. W. Murray, R. C. Thunell, L. C. Peterson, F. Muller-Karger, L. Lorenzoni, Y. Astor, and R. Varela (2010), Local and regional geochemical signatures of surface sediments of the Cariaco Basin and Orinoco Delta, Venezuela, *Geology*, *38*, 159–162, doi:10.1130/G30487.1.

Medina-Elizalde, M., and D. Lea (2005), The Mid-Pleistocene Transition in the tropical Pacific, *Science*, *310*, 1009–1012, doi:10.1126/science.1115933.

Merico, A., T. Tyrrell, and P. A. Wilson (2008), Eocene/Oligocene ocean de-acidification linked to Antarctic glaciation by sea-level fall, *Nature*, *452*, 979–982, doi:10.1038/nature06853.

Nesbitt, H. W., and G. Markovics (1997), Weathering of granodioritic crust, long-term storage of elements in weathering profiles, and petrogenesis of siliciclastic sediments, *Geochim. Cosmochim. Acta*, *61*, 1653–1670, doi:10.1016/S0016-7037(97)00031-8.

Nesbitt, H. W., and G. M. Young (1982), Early Proterozoic climate and plate motions inferred from major element chemistry of lutites, *Nature*, *299*, 715–717, doi:10.1038/299715a0.

Nesbitt, H. W., et al. (1980), Chemical processes affecting alkalis and alkaline earths during continental weathering, *Geochim. Cosmochim. Acta*, *44*, 1659–1666, doi:10.1016/0016-7037(80)90218-5.

Pagani, M., J. C. Zachos, F. Katherine, B. Tipple, and S. Bohaty (2005), Marked decline in atmospheric carbon dioxide concentrations during the Paleogene, *Science*, *309*, 600–603, doi:10.1126/science.1110063.

Paillard, D., L. Labeyrie, and P. Yiou (1996), Macintosh program performs time-series analysis, *Eos Trans. AGU*, *77*, 379, doi:10.1029/96EO00259.

Pälike, H., R. D. Norris, J. O. Herrle, P. A. Wilson, H. K. Coxall, C. H. Lear, N. J. Shackleton, A. K. Tripati, and B. S. Wade (2006), The heartbeat of the Oligocene climate system, *Science*, *314*, 1894–1898, doi:10.1126/science.1133822.

Petit, J. R., et al. (1999), Climate and atmospheric history of the past 420000 years from the Vostok ice core, Antarctica, *Nature*, *399*, 429–436, doi:10.1038/20859.

Raymo, M. E., and W. F. Ruddiman (1992), Tectonic forcing of late Cenozoic climate, *Nature*, *359*, 117–122, doi:10.1038/359117a0.

Raymo, M. E., W. F. Ruddiman, and P. N. Froelich (1988), Influence of late Cenozoic mountain building on ocean geochemical cycles, *Geology*, *16*, 649–653, doi:10.1130/0091-7613(1988)016<0649:IOLCMB>2.3.CO;2.

Richter, T. O., S. van der Gaast, B. Koster, A. Vaars, R. Gieles, H. C. de Stigter, H. de Haas, and T. C. E. van Weering (2006), The Avaatech XRF Core Scanner: Technical description and applications to NE Atlantic sediments, *Geol. Soc. Spec. Publ.*, *267*, 39–50, doi:10.1144/GSL.SP.2006.267.01.03.

Sendjaja, Y. A., and J.-I. Kimura (2010), Geochemical variation in Tertiary–Quaternary lavas of the West Java arc, Indonesia steady-state subduction over the past 10 million years, *J. Mineral. Petrol. Sci.*, *105*, 20–28, doi:10.2465/jmps.080930.

Shackleton, N. J. (1987), The carbon isotope record of the Cenozoic: History of organic carbon burial and oxygen in the ocean and atmosphere, *Geol. Soc. Spec. Publ.*, *26*, 423–434, doi:10.1144/GSL.SP.1987.026.01.27.

Shackleton, N. J. (2000), The 100,000-year ice-age cycle identified and found to lag temperature, carbon dioxide, and orbital eccentricity, *Science*, *289*, 1897–1902, doi:10.1126/science.289.5486.1897.

Shevenell, A. E., K. P. Kennett, and D. W. Lea (2004), Middle Miocene Southern Ocean cooling and Antarctic cryosphere expansion, *Science*, *305*, 1766–1770, doi:10.1126/science.1100061.

Shevenell, A. E., J. P. Kennett, and D. W. Lea (2008), Middle Miocene ice sheet dynamics, deep-sea temperatures, and carbon cycling: A Southern Ocean perspective, *Geochem. Geophys. Geosyst.*, *9*, Q02006, doi:10.1029/2007GC001736.

Siegenthaler, U., et al. (2005), Stable carbon cycle–climate relationship during the late Pleistocene, *Science*, *310*, 1313–1317, doi:10.1126/science.1120130.

Sun, Y., Z. An, S. Clemens, Y. Bloemendal, and J. Vandenberghe (2010), Seven million years of wind and precipitation variability on the Chinese Loess Plateau, *Earth Planet. Sci. Lett.*, *297*, 525–535, doi:10.1016/j.epsl.2010.07.004.

Tian, J., P. Wang, X. Cheng, and Q. Li (2002), Astronomically tuned Plio-Pleistocene benthic δ^{18}O records from South China Sea and Atlantic-Pacific comparison, *Earth Planet. Sci. Lett.*, *203*, 1015–1029, doi:10.1016/S0012-821X(02)00923-8.

Tian, J., P. X. Wang, and X. R. Chen (2004), Development of the east Asian monsoon and Northern Hemisphere glaciation: Oxygen isotope records from the South China Sea, *Quat. Sci. Rev.*, *23*, 2007–2016, doi:10.1016/j.quascirev.2004.02.013.

Tian, J., P. Wang, R. Chen, and X. Cheng (2005), Quaternary upper ocean thermal gradient variations in the South China Sea: Implications for east Asian monsoon climate, *Paleoceanography*, *20*, PA4007, doi:10.1029/2004PA001115.

Tian, J., D. Pak, P. X. Wang, D. Lea, X. R. Cheng, and Q. Zhao (2006), Late Pliocene monsoon linkage in the tropical South China Sea, *Earth Planet. Sci. Lett.*, *252*, 72–81, doi:10.1016/j.epsl.2006.09.028.

Tian, J., Q. Zhao, P. Wang, Q. Li, and X. Cheng (2008), Astronomically modulated Neogene sediment records from the South China Sea, *Paleoceanography*, *23*, PA3210, doi:10.1029/2007PA001552.

Tian, J., A. Shevenell, P. Wang, Q. Zhao, Q. Li, and X. Cheng (2009), Reorganization of Pacific deep waters linked to middle Miocene Antarctic cryosphere expansion: A perspective from the South China, *Palaeogeogr. Palaeoclimatol. Palaeoecol.*, *284*, 375–382, doi:10.1016/j.palaeo.2009.10.019.

Tiedemann, R., M. Sarnthein, and N. J. Shackleton (1994), Astronomic timescale for the Pliocene Atlantic δ^{18}O and dust flux records from Ocean Drilling Program Site 659, *Paleoceanography*, *9*, 619–638, doi:10.1029/94PA00208.

Tjallingii, R., U. Röhl, M. Kölling, and T. Bickert (2007), Influence of the water content on X-ray fluorescence core-scanning measurements in soft marine sediments, *Geochem. Geophys. Geosyst.*, *8*, Q02004, doi:10.1029/2006GC001393.

Wade, B. S., and H. Pälike (2004), Oligocene climate dynamics, *Paleoceanography*, *19*, PA4019, doi:10.1029/2004PA001042.

Walker, J. C. G., and J. F. Kasting (1992), Effects of fuel and forest conservation on future levels of atmospheric carbon dioxide, *Global Planet. Change*, *5*(3), 151–189, doi:10.1016/0921-8181(92)90009-Y.

Wan, S. M., A. C. Li, P. D. Clift, and H. Y. Jiang (2006), Development of the East Asian summer monsoon: Evidence from the sediment record in the South China Sea since 8.5 Ma, *Palaeogeogr. Palaeoclimatol. Palaeoecol.*, *241*, 139–159, doi:10.1016/j.palaeo.2006.06.013.

Wang, L., M. Sarnthein, H. Erlenkeuser, J. Grimalt, P. Grootes, S. Heilig, E. Ivanova, M. Kienast, C. Pelejero, and U. Pflaumann (1999), East Asian monsoon climate during the late Pleistocene: High-resolution sediment records from the South China Sea, *Mar. Geol.*, *156*, 245–284, doi:10.1016/S0025-3227(98)00182-0.

Wang, P., W. L. Prell, and P. Blum (2000), *Proceedings of the Ocean Drilling Program, Initial Reports*, vol. 184, Ocean Drill. Program, College Station, Tex.

Wang, P., J. Tian, and X. R. Cheng (2001), Transition of Quaternary glacial cyclicity in deep-sea records at Nansha, the South China Sea, *Sci. China, Ser. D*, *44*(10), 926–933, doi:10.1007/BF02907085.

Wang, P., J. Tian, X. Cheng, C. Liu, and J. Xu (2004), Major Pleistocene stages in a carbon perspective: The South China Sea record and its global comparison, *Paleoceanography*, *19*, PA4005, doi:10.1029/2003PA000991.

Wang, P., J. Tian, and L. Lourens (2010), Obscuring of long eccentricity cyclicity in Pleistocene oceanic carbon isotope records, *Earth Planet. Sci. Lett.*, *290*, 319–330, doi:10.1016/j.epsl.2009.12.028.

Wara, M. W., A. C. Ravelo, and M. L. Delaney (2005), Permanent El Niño–like conditions during the Pliocene warm period, *Science*, *309*, 758–761, doi:10.1126/science.1112596.

Wehausen, R., and H. Brumsack (2002), Astronomical forcing of the East Asian monsoon mirrored by the composition of Pliocene South China Sea sediments, *Earth Planet. Sci. Lett.*, *201*, 621–636, doi:10.1016/S0012-821X(02)00746-X.

Wehausen, R., et al. (2003), Geochemistry of Pliocene sediments from ODP Site 1143 (southern South China Sea), *Proc. Ocean Drill. Program Sci. Results*, *184* [Online].

Wei, G., X.-H. Li, Y. Liu, L. Shao, and X. Liang (2006), Geochemical record of chemical weathering and monsoon climate change since the early Miocene in the South China Sea, *Paleoceanography*, *21*, PA4214, doi:10.1029/2006PA001300.

Weltje, G. J., and R. Tjallingii (2008), Calibration of XRF core scanners for quantitative geochemical logging of sediment cores: Theory and application, *Earth Planet. Sci. Lett.*, *274*(3–4), 423–438, doi:10.1016/j.epsl.2008.07.054.

Westerhold, T., U. Röhl, J. Laskar, I. Raffi, J. Bowles, L. J. Lourens, and J. C. Zachos (2007), On the duration of magnetochrons C24r and C25n and the timing of early Eocene global warming events: Implications from the Ocean Drilling Program Leg 208 Walvis Ridge depth transect, *Paleoceanography*, *22*, PA2201, doi:10.1029/2006PA001322.

Yancheva, G., et al. (2007), Influence of the intertropical convergence zone on the East Asian monsoon, *Nature*, *445*, 74–77, doi:10.1038/nature05431.

Yarincik, K. M., R. W. Murray, and L. C. Peterson (2000), Climatically controlled eolian and hemipelagic deposition in the Cariaco Basin, Venezuela, over the past 578,000 years: Results from Al/Ti and K/Al, *Paleoceanography*, *15*, 210–228, doi:10.1029/1999PA900048.

Zachos, J., M. Pagani, L. C. Sloan, E. Thomas, and K. Billups (2001), Trends, rhythms, and aberrations in global climate 65 Ma to present, *Science*, *292*, 686–693, doi:10.1126/science.1059412.

Zhang, P. Z., P. Molnar, and W. R. Downs (2001), Increased sedimentation rates and grain sizes 2–4 Myr ago due to the influence of climate change on erosion rates, *Nature*, *410*, 891–897, doi:10.1038/35073504.

Zheng, H. B., C. M. Powell, D. K. Rea, J. L. Wang, and P. X. Wang (2004), Late Miocene and mid-Pliocene enhancement of the East Asian monsoon as viewed from the land and sea, *Global Planet. Change*, *41*, 147–155, doi:10.1016/j.gloplacha.2004.01.003.

H. Jin, W. Ma, J. Tian, P. Wang, and X. Xie, State Key Laboratory of Marine Geology, Tongji University, 1239 Siping Rd., Shanghai 200092, China. (tianjun@tongji.edu.cn)